

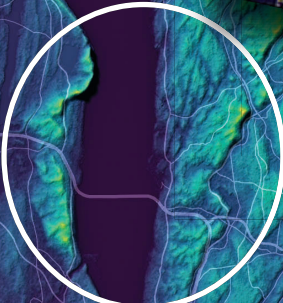
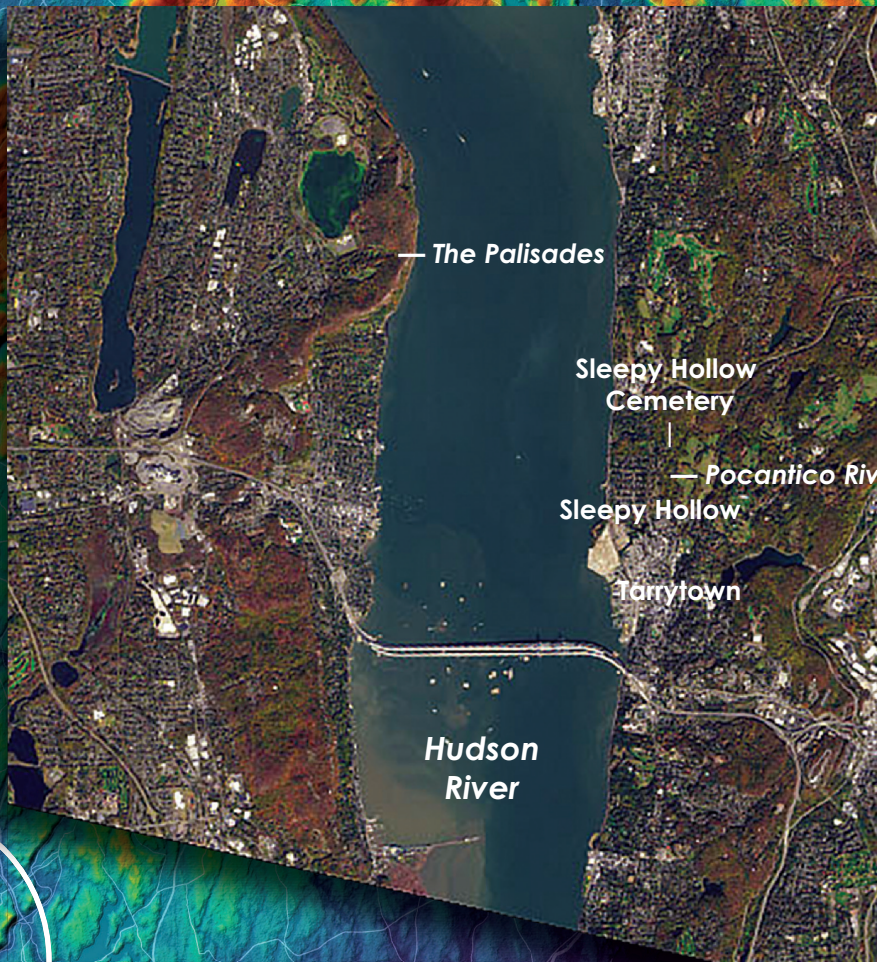
PE&RS

October 2022

Volume 88, Number 10

The official journal for imaging and geospatial information science and technology

PHOTOGRAMMETRIC ENGINEERING & REMOTE SENSING



PECORA 22

Opening the
Aperture to Innovation:
Expanding Our Collective
Understanding of a
Changing Earth

William T. Pecora Remote Sensing Symposium

OCTOBER 24 — 27, 2022 Denver, Colorado, USA

The premier symposium focusing on all aspects of Earth observations, spanning scientific discoveries to operational applications, sensors, and decisions. Pecora 22 embraces both innovation and discovery while Landsat data improves our ability to understand and better manage the resources of our Earth's surface.

Celebrating

50

YEARS

Landsat

1972-2022

2022 marks the 50th anniversary of the launch of the first Landsat satellite.

Join us as we celebrate 50 years of accomplishments, innovations, and discoveries— all with an eye on the future.

For more information on the conference, program line-up, and to register, visit Pecora22.org.

ANNOUNCEMENTS

NV5 Geospatial announced the debut of its ARIS II Rover. The upgraded robotic electric substation monitoring system comes after five years of in-field implementation and testing. The rover meets the industry's most exacting standards for ruggedness and reliability, enabling it to function in harsh environmental conditions and over various terrains commonly found at distribution and transmission substations. The remotely controlled wheeled rover offers a modular design custom-fitted with advanced thermal sensors, imaging, and audio/video technology that allows utilities to protect assets and limit liability while speeding reaction time.

"Geographic and personnel limitations, combined with aging infrastructure, present significant challenges for utility companies when it comes to maintaining their substations," said Ian Birdie, vice president of Innovation for NV5 Geospatial. "With our extensive experience in these substation environments, NV5 Geospatial has customized the ARIS II Rover for the unique needs of utilities. We built our next-generation robot on a rugged platform that can exist remotely and deliver the information and insights utilities need to maintain their networks proactively. On-time information allows quick response to equipment anomalies, weather events, and intrusions before they have an impact."

The ARIS II rover supports a variety of applications, including event check-ups, situational awareness, health monitoring, work audits, inventory management, emergency response and security, offering:

- Industry-leading military standards (MIL-STD) and ingress protection ratings, resulting in a weatherproof design that can withstand and work reliably in harsh environments, and 36-degree climbing ability for difficult terrain.
- Pre-configured payload of sensors and equipment that supports thermal imaging, video and two-way audio communication capabilities, as well as GPS with real-time kinematics (RTK) that supports accurate mapping of drives within a substation.
- Modular design for flexibility in sensor and camera positioning and simplified maintenance on or off site, with the ability to carry up to 110 lbs of equipment.
- Up to six hours of battery life or two miles of driving and a recharge garage included when the rover is not in use.
- Easy installation and movement to different substation locations with a pallet-ready Rover and housing.
- Secure web portal that offers controls and management tools to support real-time inspection/driving, feedback and measurement from onboard sensors, and the ability to review and measure thermal conditions and high-resolution photos.

This combination of features enables the ARIS II Rover to assess conditions in substations. Thermal imaging captures

temperature deltas against assets to help utilities determine when equipment needs to be evaluated and replaced. Onboard cameras can visually detect corrosion and asset damage, and are able to read gauges from up to 50 feet away.

To learn more about the ARIS II Rover or to schedule a demonstration, contact NV5G-Sales@nv5.com.



Trimble announced today its commitment to reduce greenhouse gas emissions in line with the ambitious goals of the Paris Agreement and a net-zero future to keep global temperature increase to 1.5°C. Trimble received approval of its emissions reduction targets by the Science Based Targets initiative (SBTi), a coalition of the CDP, the United Nations Global Compact, World Resources Institute and the World Wide Fund for Nature, joining a growing number of companies taking urgent action on climate change.

"Taking decisive climate action is essential to protect our planet and communities for future generations. It also demonstrates Trimble's commitment to our purpose—to transform the way the world works as well as transform the way "we" work," said Rob Painter, president and CEO, Trimble.

"For decades, Trimble solutions have contributed to reducing greenhouse gas emissions and combating climate change," continued Painter. "The nature of Trimble's technologies, which connect the physical and digital worlds, provides efficiencies and promotes sustainability in our end markets such as construction, agriculture, forestry, utilities and transportation. Our leadership team is committed to further reducing our carbon footprint as well as continuing to develop solutions that enable our customers to reduce their climate impacts—it is an important lever in our Connect and Scale strategy. Trimble is dedicated to do its part to help protect and build a better world."

Trimble's science-based targets accelerate decarbonization across its value chain, and include the following commitments:

- Reduce absolute scope 1 and 2 greenhouse gas emissions 50 percent by 2030 from a 2019 base year
- Achieve 100 percent annual sourcing of renewable electricity by 2025
- Reduce absolute scope 3 greenhouse gas emissions from fuel and energy related activities, business travel and upstream transportation and distribution 50 percent by 2030 from a 2019 base year
- Commit to partner with 70 percent of its suppliers by emissions covering purchased goods and services and capital goods to set science-based targets by 2026.

This decade is considered the decisive decade for climate

change. As part of answering this urgent call to action, Trimble has joined forces with other companies and climate leaders in the Business Ambition for 1.5°C campaign, the We Mean Business Coalition and the Race to Zero Campaign.

“Setting ambitious yet achievable climate targets are part of our commitment to reducing Trimble’s carbon footprint,” said Leah Lambertson, senior vice president and head of Sustainability, Trimble. “Embedding our climate action goals into Trimble’s operational choices will help ensure that our decision making and growth plans are consistent with our low-carbon vision. Today’s commitments are important steps in our journey to delivering growth in a responsible and sustainable way to achieve a net-zero future.”

Trimble also announced the release of its 2021 Sustainability Report. Built around the company’s mission of transforming the way the world works, the report features how Trimble is helping to create a better future for our planet and the communities we serve.

The report summarizes its initiatives and performance across Environmental, Social and Governance (ESG) topics, highlighting the company’s sustainability approach; end-user industry solutions; community philanthropy through its Trimble Foundation Fund; employee engagement and development as well as Diversity, Equity and Inclusion (DEI) initiatives; and governance.



URISA is pleased to announce the results of its 2022 URISA Board of Directors’ election. Tom Fisher will serve in the position of President-Elect and Josiah Burkett, Bernadette deLeon, and Matt Gerike will serve as Directors. They will all begin their three-year terms at the conclusion of GIS-Pro 2022 in Boise.

Tom will serve as President-Elect for one year and his term as President will begin at the conclusion of GIS-Pro 2023.

“This is a great honor to lead the URISA organization and

to represent the members for three more years through the Presidential track. URISA has accomplished a lot over the past sixty years with steady leadership and member volunteerism. I plan to continue the tradition of excellence set by the trailblazers before me and leave a legacy of servant leadership for upcoming geospatial professionals to aspire to. Thank you again for your confidence and trust to lead URISA. I look forward to seeing everyone in Boise, Idaho this fall and, in the chapters, and committees of this amazing URISA organization.”

Newly-elected URISA Directors include:

- Josiah Burkett, Geographic Information Systems Analyst /Geospatial Team Lead, GeoTechVision, Kingston, Jamaica
- Bernadette de Leon, GISP, Director of School of Public Health Bloomington IT Services
Indiana University, Bloomington, Indiana
- Matthew J. Gerike, PhD, GISP, Geospatial Program Manager, Virginia Geographic Information Network (VGIN), Virginia Department of Emergency Management (VDEM), Richmond, Virginia

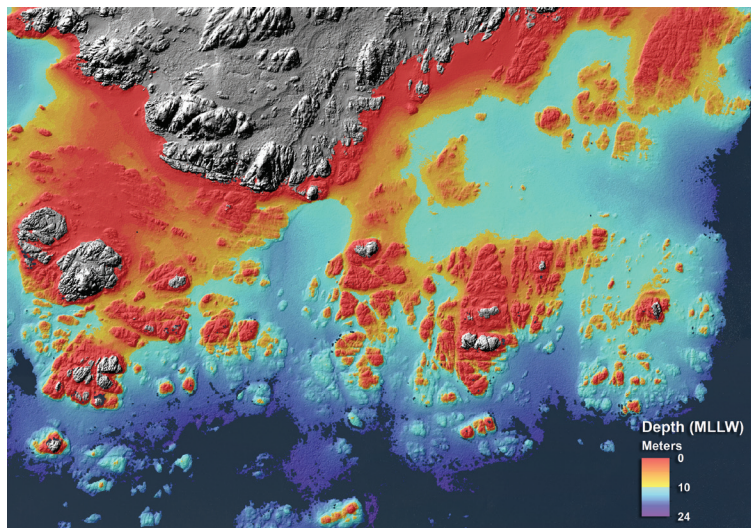
Ashley Hitt was elected by the membership as President-Elect last year and will begin her term as President of URISA at the conclusion of GIS-Pro 2022. Brent Jones will become Immediate Past-President at that time.

At the close of GIS-Pro 2022, the terms of service for these URISA Board members will conclude and we thank them all, in advance, for their amazing dedication and service to URISA:

- Immediate Past President—Kevin Mickey, GISP, The Polis Center-IUPUI, Indianapolis, Indiana
- Board Secretary—Susan Kamei, USC Spatial Sciences Institute - Los Angeles, California
- Tom Fisher, GISP, AICP, Cuyahoga County - Cleveland, Ohio
- John Nolte, GISP, Denver Water - Denver, Colorado

CALENDAR

- 23-27 October, **Pecora 22**, Denver, Colorado. For more information, visit <https://pecora22.org/>.
- 31 October - 4 November, **URISA GIS Leadership Academy**, Santa Rosa, California. For more information, visit www.urisa.org/education-events/urisa-gis-leadership-academy/.
- 2-4 November, **AutoCarto 2022— Ethics in Mapping: Integrity, Inclusion, and Empathy**, Redlands, California. For more information, visit <https://cartogis.org/autocarto/autocarto-2022/>.



617 How to Gain Clearer Visibility into Dynamic Coastal Environments

By Alexa Ramirez, PMP, GISP, and Colin Cooper, GISP, NV5 Geospatial

COLUMNS

- 621** GIS Tips & Tricks — Need a Custom USGS Topo Map? Here is How to Make it Yourself!
- 627** Grids and Datums
This month we look at Grenada

ANNOUNCEMENTS

- 626** ASPRS Certifications
- 629** Headquarters News—ASPRS Estes Teaching Excellence Award: Call for Nominations
- 629** New ASPRS Members
Join us in welcoming our newest members to ASPRS.
- 630** Call for *PE&RS* Special Issue Submissions — Innovative Methods for Geospatial Data using Remote Sensing and GIS

DEPARTMENTS

- 613** Industry News
- 614** Calendar
- 626** Ad Index
- 652** In-Press *PE&RS* Articles
- 672** ASPRS Sustaining Members

631 A Novel Residual Attitude Estimation Approach Using Georeferenced Satellite Imagery

Bhaskar Dubey and B. Kartikeyan

This article presents an efficient novel approach estimating residual attitude based on geometrically corrected (GEO) satellite images. A technique is presented that uses orbital plane geometry to compute the rotation angle as a function of geographic latitude between GEO image space and radiometrically corrected (RAD) image space.

643 Efficient Building Inventory Extraction from Satellite Imagery for Megacities

Edmond Yat-Man Lo, En-Kai Lin, Velautham Daksiya, Kuo-Shih Shao, Yi-Rung Chuang, and Tso-Chien Pan

Accurate building inventories are essential for city planning and disaster risk management. Traditionally generated via census or selected small surveys, these suffer from data quality and/or resolution. High-resolution satellite imagery with object segmentation provides an effective alternative, readily capturing large extents. This article develops a highly automated building extraction methodology for location-based building exposure data from high (0.5 m) resolution satellite stereo imagery.

653 A Semi-Supervised Learning Method for Hyperspectral-Image Open Set Classification

Zhaolin Duan, Hao Chen, Xiaohua Li, Jiliu Zhou, and Yuan Wang

We present a conceptually simple and flexible method for hyperspectral-image open set classification. Unlike previous methods, where the abundant unlabeled data inherent in the data set are ignored completely and unknown classes are inferred using score post-calibration, our approach makes the unlabeled data join in and help to train a simple and practical model for open set classification. The model is able to provide an explicit decision score for both unknown classes and each known class.

655 The Fractional Vegetation Cover (FVC) and Associated Driving Factors of Modeling in Mining Areas

Jun Li, Tianyu Guo, Chengye Zhang, Fei Yang, and Xiao Sang

To determine the fractional vegetation cover (FVC) and associated driving factors of modeling in mining areas, six types of data were used as driving factors and three methods—multi-linear regression (MLR), geographically weighted regression (GWR), and geographically weighted artificial neural network (GWANN)—were adopted in the modeling.

See the Cover Description on Page 616

COVER DESCRIPTION

In 1798, with a yellow fever epidemic raging in New York City, fifteen-year-old Washington Irving was sent north to stay with a family friend in the lower Hudson River Valley in the hope that fresh air and open space would help him elude the deadly virus. He ended up in Tarrytown, a small town about 25 miles (40 kilometers) north of Manhattan on the eastern side of the river.

Irving delighted in exploring the verdant, rocky landscapes north of Tarrytown, particularly an area later named Sleepy Hollow. He found the forests and streams there to be perfect for wandering, daydreaming, and fishing. He later settled there, and many of the landscapes he had explored as a teen became nostalgic backdrops for his short stories.

One of his most famous—The Legend of Sleepy Hollow—is set in the area highlighted in the cover image. The image is composed from elevation data from the Shuttle Radar Topography Mission (SRTM). It is false-color to emphasize the topography; red areas are the highest elevations, and blue areas are closer to sea level. The Operational Land Imager (OLI) on Landsat 8 acquired a natural-color image (below) of the same area on October 27, 2017.

Much of the rock beneath this landscape is Fordham gneiss, an ancient bedrock that formed more than one billion years ago under the intense heat and pressure of colliding land masses. The smashing and suturing of continents that produced a supercontinent called Rodinia was followed by countless cycles of erosion, mountain building, and the ebb and flow of ice ages. Over time, these and other geologic processes formed the worn, hilly landscapes that are found today around Sleepy Hollow.

According to Irving's tale, the forests and swamps of this uneven, corrugated terrain are where a headless horseman—perhaps a Hessian soldier killed during the Revolutionary War—is said to roam at night looking for his missing head. The Sleepy Hollow Cemetery and Old Dutch Church, landmarks that feature prominently in the story, sit on a small ridge near the center of the image.

The Pocantico River, what Irving calls that "wizard stream," flows through a valley that appears as a dark, thin line in the elevation map. In the story's climax, the Headless Horseman chases the protagonist across a wooden bridge over the river. To the east, in the Pocantico Hills, lies Raven Rock, a large glacial erratic transported and deposited by melting ice in a glen haunted by the ghost of a woman who perished there. The cliff on the western side of the river, part of the Palisades, formed roughly 200 million years ago when a sheet of rising magma was trapped between layers of sedimentary rock as a different supercontinent was breaking apart.

Irving died and was buried in the Sleepy Hollow Cemetery in 1859, but his words about Sleepy Hollow live on. They still resonate, especially on Halloween, when the town celebrates its literary history with a festival each year. "The place still continues under the sway of some witching power, that holds a spell over the minds of the good people, causing them to walk in a continual reverie," Irving wrote in the opening of *The Legend of Sleepy Hollow*. "The whole neighborhood abounds with local tales, haunted spots, and twilight superstitions; stars shoot and meteors glare oftener across the valley than in any other part of the country, and the nightmare, with her whole ninefold, seems to make it the favorite scene of her gambols."

Visit, <https://landsat.visibleearth.nasa.gov/view.php?id=149022> to see both images in full size.

NASA Earth Observatory images by Joshua Stevens. using topographic data from the Shuttle Radar Topography Mission (SRTM) and Landsat data from the U.S. Geological Survey. Story by Adam Voiland.



PHOTOGRAMMETRIC ENGINEERING & REMOTE SENSING

JOURNAL STAFF

Publisher ASPRS

Editor-In-Chief Alper Yilmaz

Director of Publications Rae Kelley

Electronic Publications Manager/Graphic Artist

Matthew Austin

Photogrammetric Engineering & Remote Sensing is the official journal of the American Society for Photogrammetry and Remote Sensing. It is devoted to the exchange of ideas and information about the applications of photogrammetry, remote sensing, and geographic information systems. The technical activities of the Society are conducted through the following Technical Divisions: Geographic Information Systems, Photogrammetric Applications, Lidar, Primary Data Acquisition, Professional Practice, Remote Sensing Applications, and Unmanned Autonomous Systems Division. Additional information on the functioning of the Technical Divisions and the Society can be found in the Yearbook issue of *PE&RS*.

Correspondence relating to all business and editorial matters pertaining to this and other Society publications should be directed to the American Society for Photogrammetry and Remote Sensing, 8550 United Plaza Boulevard, Suite 1001, Baton Rouge, LA 70809, including inquiries, memberships, subscriptions, changes in address, manuscripts for publication, advertising, back issues, and publications. The telephone number of the Society Headquarters is 301-493-0290; the fax number is 225-408-4422; web address is www.asprs.org.

PE&RS. *PE&RS* (ISSN0099-1112) is published monthly by the American Society for Photogrammetry and Remote Sensing, 425 Barlow Place, Suite 210, Bethesda, Maryland 20814-2144. Periodicals postage paid at Bethesda, Maryland and at additional mailing offices.

SUBSCRIPTION. For the 2022 subscription year, ASPRS is offering two options to our *PE&RS* subscribers — an e-Subscription and the print edition. e-Subscribers can add printed copies to their subscriptions for a small additional charge. Print and Electronic subscriptions are on a calendar-year basis that runs from January through December. We recommend that customers who choose print and e-Subscription with print renew on a calendar-year basis.

The rate for a Print subscription for the USA is \$1105.00 USD, for Canadian* is \$1164.00 USD, and for Non-USA is \$1235.00 USD.

The rate for e-Subscription (digital) Site License for the USA and Non-USA is \$1040.00 USD and for Canadian* is \$1089.00 USD.

The rate for e-Subscription (digital) plus Print for the USA is \$1405.00 USD, for Canadian* is \$1464.00 USD, and for Non-USA is \$1435.00 USD.

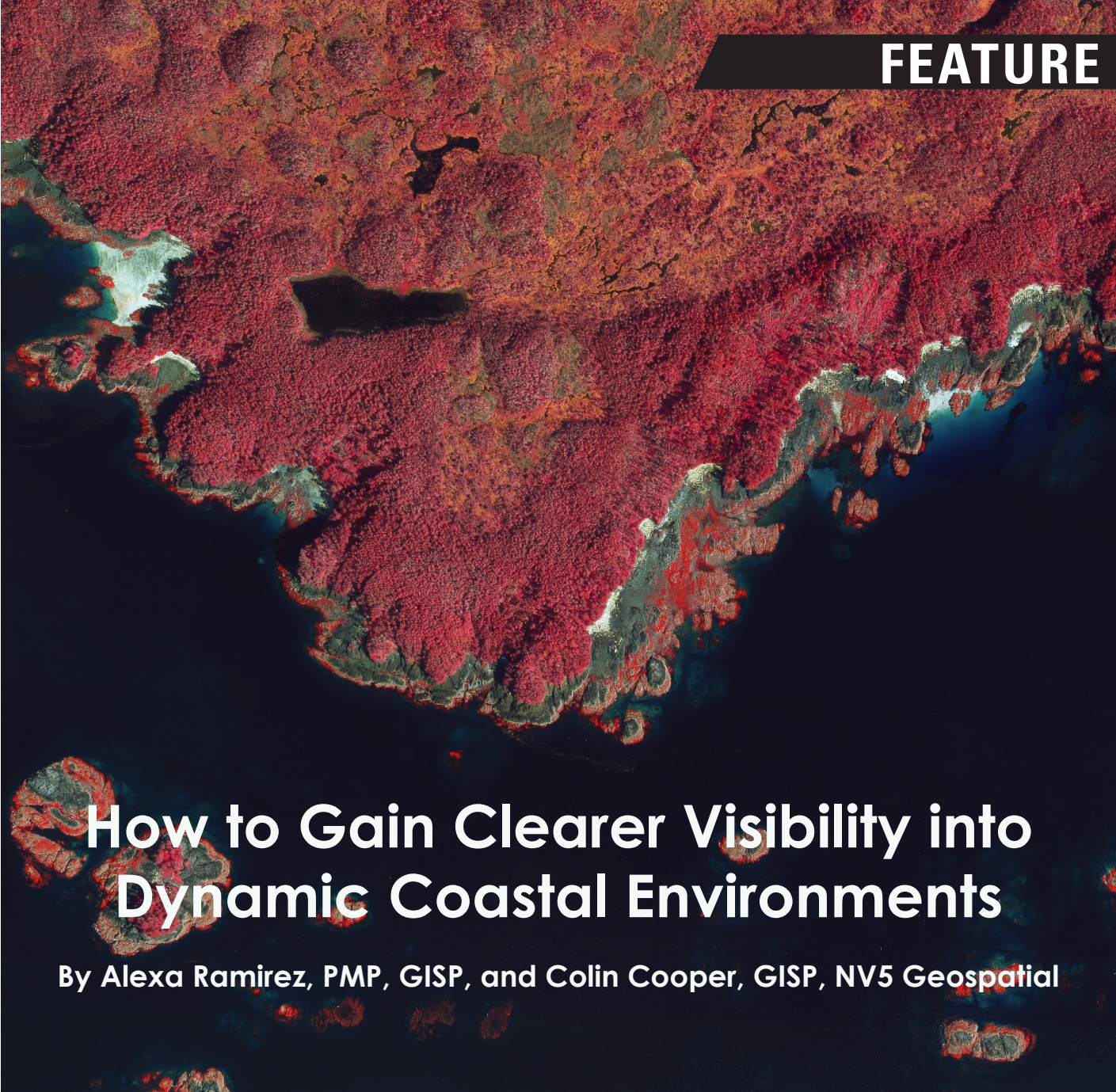
*Note: e-Subscription, Print subscription, and e-Subscription plus Print for Canada includes 5% of the total amount for Canada's Goods and Services Tax (GST #135123065). **PLEASE NOTE: All Subscription Agencies receive a 20.00 USD discount.**

POSTMASTER. Send address changes to *PE&RS*, ASPRS Headquarters, 8550 United Plaza Boulevard, Suite 1001, Baton Rouge, LA 70809. CDN CPM #40020812).

MEMBERSHIP. Membership is open to any person actively engaged in the practice of photogrammetry, photointerpretation, remote sensing and geographic information systems; or who by means of education or profession is interested in the application or development of these arts and sciences. Membership is for one year, with renewal based on the anniversary date of the month joined. Membership Dues include a 12-month electronic subscription to *PE&RS*. To receive a print copy of *PE&RS* there is an additional postage fee of \$60.00 USD for U.S. shipping; \$65.00 USD for Canadian shipping; or \$75.00 USD for international shipping per year. Annual Individual Member dues for members residing in the U.S. and Other Foreign Members are \$150.00 USD and \$158.00 USD for Canadians. Annual Student Member dues for members residing in the U.S. are \$50.00 USD; \$53.00 USD for Canadian; and \$60.00 USD for Other Foreign Members. A tax of 5% for Canada's Goods and Service Tax (GST #135123065) is applied to all members residing in Canada.

COPYRIGHT 2022. Copyright by the American Society for Photogrammetry and Remote Sensing. Reproduction of this issue or any part thereof (except short quotations for use in preparing technical and scientific papers) may be made only after obtaining the specific approval of the Managing Editor. The Society is not responsible for any statements made or opinions expressed in technical papers, advertisements, or other portions of this publication. Printed in the United States of America.

PERMISSION TO PHOTOCOPY. The copyright owner's consent that copies of the article may be made for personal or internal use or for the personal or internal use of specific clients. This consent is given on the condition, however, that the copier pay the stated per copy fee through the Copyright Clearance Center, Inc., 222 Rosewood Drive, Danvers, Massachusetts 01923, for copying beyond that permitted by Sections 107 or 108 of the U.S. Copyright Law. This consent does not extend to other kinds of copying, such as copying for general distribution, for advertising or promotional purposes, for creating new collective works, or for resale.



How to Gain Clearer Visibility into Dynamic Coastal Environments

By Alexa Ramirez, PMP, GISP, and Colin Cooper, GISP, NV5 Geospatial

Mapping rugged coastlines is dangerous work. Rocky shores, underwater hazards, volatile weather, and changing turbidity create perilous conditions. These conditions make it difficult to collect accurate, detailed data through conventional means, including boats equipped with sonar and ground survey instruments.

Advances in technology are changing the dynamics. Using a state-of-the-art combination of advanced remote sensing and imaging technologies, NV5 Geospatial is yielding more accurate data and delivering insights on dynamic coastal landscapes.

Figure 1 (above). Color infrared image of the southern end of Duke Island. Duke Island is part of the Alexander Archipelago in southeastern Alaska. Image is created from 4 band imagery collected with the Vexcel UltraCam Eagle M3 camera.

A History of Innovation

NV5 Geospatial is no stranger to challenging geospatial projects. Throughout our company's 90+ year history, we have been at the center of many of the nation's most interesting and demanding projects.

NV5 Geospatial and its predecessor companies documented the construction of the Golden Gate Bridge in the '30s and mapped the Colorado River in the Grand Canyon, flying more than 3000 feet below the rim in many locations. We performed the first ever comprehensive mapping of Ameri-

Photogrammetric Engineering & Remote Sensing
Vol. 88, No. 10, October 2022, pp. 617-619.
0099-1112/22/617-619

© 2022 American Society for Photogrammetry
and Remote Sensing
doi: 10.14358/PERS.88.10.617

can Samoa's five islands and two atolls and monitored the eruption of Kilauea in Hawaii and its impact on the local population and environment. In addition, we conducted the largest hyperspectral project on record, providing accurate locations of all ash trees in and around electric grid assets and documenting risk from the emerald ash borer.

The secret to NV5 Geospatial's success on projects of this scale is our constant innovation, seeking a diversity of cutting-edge geospatial technologies and solutions that deliver more and better data. In just the past decade, we have become well known for our expertise in ship-based bathymetric surveys and topobathymetric lidar.

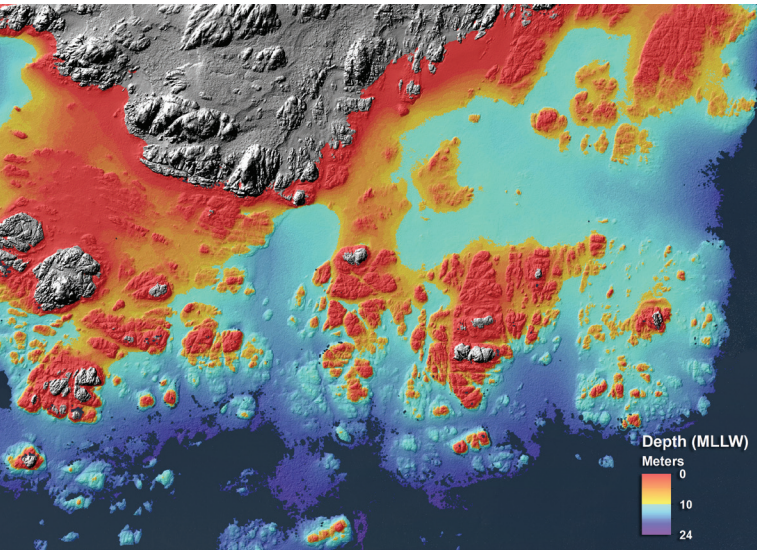


Figure 2. Hillshade model of the topobathymetric lidar generated DEM colored by depth to highlight areas shallower than 10 meters. Submerged rocks and a steeply rising coastline make this area dangerous and difficult to map with survey vessels.

Alaska Topobathymetric Project Breaks New Ground

The Alaska Coastal Mapping Strategy was spearheaded by the 2019 Presidential Memorandum on Ocean Mapping of the United States Exclusive Economic Zone and the Shoreline and Nearshore of Alaska, which brought together the National Oceanic and Atmospheric Administration (NOAA), the State of Alaska, and the Alaska Coastal Mapping Executive Committee. The long-term vision was to create seamless coastal mapping data across the state of Alaska by 2030, with short-term goals of prioritized topobathymetric lidar mapping campaigns that build a strong connection between land and sea.

NV5 Geospatial's contribution to this initiative began with mapping the coastal waters of the Revillagigedo Channel in Alaska for NOAA's National Geodetic Survey (NGS) Remote Sensing Division (RSD) Coastal Mapping Program (CMP). NOAA, and its partners at the State of Alaska and the Alaska Coastal Mapping Executive Committee, brought in NV5 Geospatial to leverage our unique array of sensors and processes. The project required planning and executing an 846-square-mile aerial acquisition, which began in June 2021, and was conducted as weather permitted. We also deployed buoys throughout the survey area to monitor water turbidity and performed limited ground surveys.

The Coastal Mapping Program requires the collection of airborne topographic/bathymetric lidar and digital camera imagery data to enable accurate and consistent measurement of the national shoreline. This supports increasing efficiency and safety of NOAA's hydrographic surveying operations and is critical for updating nautical charts, managing coastal resources, and defining U.S. territorial limits.

Conditions in and around the Revillagigedo Channel make it extremely difficult and hazardous to operate large survey vessels in nearshore areas. There is a short operational window for data collection due to environmental constraints in addition to shoals and rocky outcrops that must be avoided. This is mitigated by collecting topobathymetric lidar in the dangerous, hard-to-reach areas where the rocky shoreline meets the open water. The lidar data allows sonar vessels to stay further offshore where they can collect data safely and efficiently.

A Closer Look at the Remote Sensing Technology

NV5 Geospatial's topobathymetric program relies on multiple lidar systems. When planning projects, we take into careful consideration how sensor selection, site characteristics, survey approach, acquisition specifications and processing methodology will impact results and data quality.

In Alaska, we deployed Leica Chiroptera 4X and Hawkeye 4X topobathymetric lidar sensors for mapping submerged lands, a Riegl VQ1560ii near-infrared (NIR) topographic lidar sensor for mapping adjacent lands, and a Vexcel Ultra-Cam Eagle M3 camera for four-band imagery acquisition - all installed in a fixed-wing aircraft. The Chiroptera/HawkEye 4x combines shallow- and deep-water laser channels that produce high-resolution and accurate data necessary for detecting submerged features. It has an integrated NIR channel for capturing seamless data at the land water interface. Southeast Alaska is characterized by mountainous terrain, fjords, and boxed canyons that can pose safety and efficiency problems for capturing the nearshore land with low altitude topobathymetric sensors. Adding the Riegl VQ1560ii supported decoupling of inland and nearshore areas, which allowed increased flight windows crucial to maximizing productivity on limited good weather days.

To support the aerial work, we needed to collect ground truthing data across the study area, which was rugged and remote. To achieve necessary coverage, we had to rely on a boat to access areas to survey. We were able to conduct real-time kinematic (RTK) GPS surveys to collect non-vegetated and vegetated vertical accuracy check points, as well as the necessary control points for both lidar and imagery processing. A boat was also used to deploy buoys equipped with Xylem EXO2 turbidity sondes to provide real-time monitoring of conditions across the area. In addition, two docks were set up with turbidity monitoring stations.

Once acquired, NV5 Geospatial calibrated and processed lidar data using commercial and proprietary software to meet the national mapping program specifications. The Leica Lidar Survey Studio was used to extract points from the bathymetric waveform data, as well as define the water surface, which it uses to correct the placement of points for refracting into the water column. Additional processing steps were used to seam-



Figure 3. 3D visualization of the topobathymetric DEM colored by depth with the above ground lidar point cloud colored by color infrared imagery. The topobathymetric lidar reveals a rugged terrain under water with kelp beds that pose risk for marine traffic.

lessly combine the collected topographic data from the Riegl VQ1560ii sensor with coastal shore data collected from the Chiroptera 4x's topographic NIR channel. A detailed outline was developed between the datasets, which favored hard permanent surfaces with no to little change, mitigating artifacts in the final developed elevation models.

The average bathymetric laser penetration throughout the study area was approximately 12 meters, with maximum depths reaching down to greater than 25 meters in clearer waters. The resulting submerged topography highlighted areas of rocky outcrops, shoals, and pervasive kelp beds.



Figure 4. GPS survey set-up to collect a hard surface check point used in verifying the lidar elevation data's vertical accuracy. Ground survey operations to support this project were largely accessible only by boat.

Results Benefit A Wide Array of Applications

While this project was conducted for NOAA's coastal mapping program, the data collected will be far reaching in support of a variety of important applications when made available to other federal, state, local, and tribal government agencies; the private sector; not-for-profit, and the public.

For example, topobathymetric data can provide insights that:

- Support maritime trade and transportation
- Inform wave and wind energy site selection
- Contribute to coastal resiliency efforts, such as modeling sea level change, storm surge, coastal flooding, and pollution trajectories
- Help analyze and monitor the environment and critical habitats
- Assist in developing land and marine GIS base layers

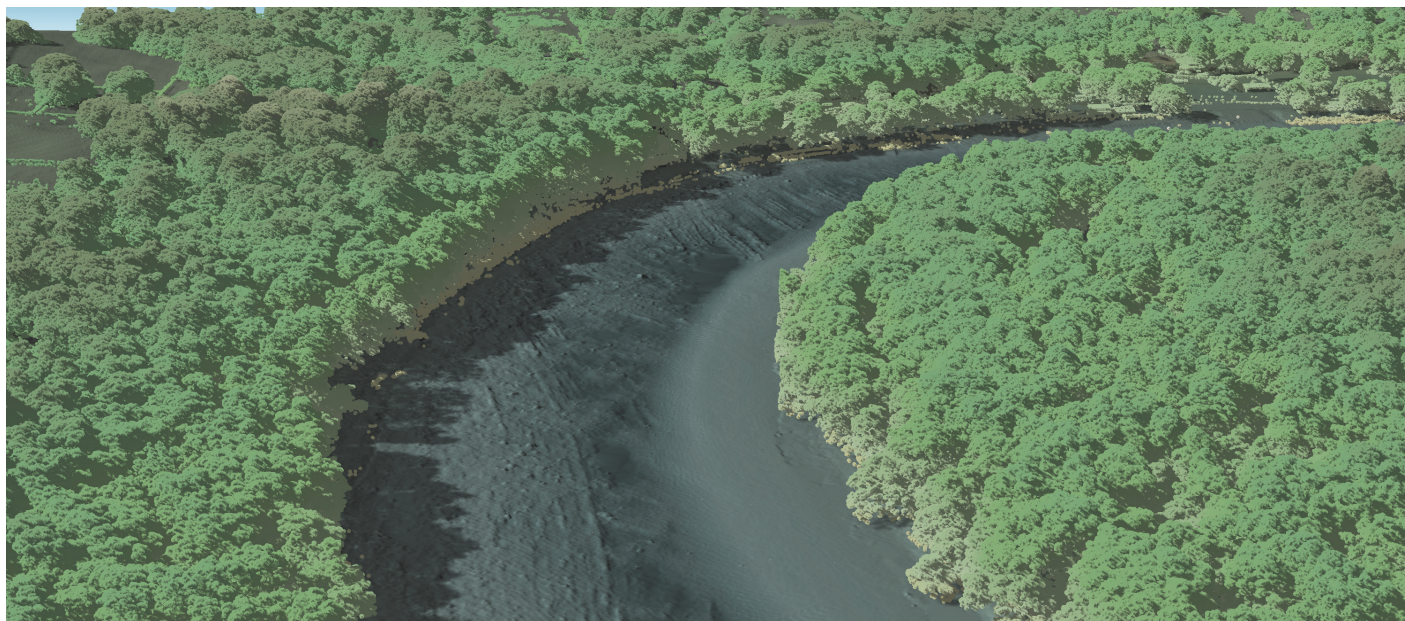
Overall, the topobathymetric lidar collected for NOAA's CMP demonstrates the strength of the technology for mapping logistically and environmentally challenging environments. The implications for supporting larger mapping efforts, such as the Alaska Coastal Mapping Initiative, cannot be understated. With careful sequencing and planning, a symbiotic relationship is formed where technologies complement each other to increase data coverage in an efficient and safe way.

If you'd like to learn more about NV5 Geospatial's work in Alaska or its topobathymetric capabilities, visit nv5geospatial.com.

About the Authors

Alexa Ramirez is an eGIS Program Manager for NV5 Geospatial. She is certified as a PMP and GISP and holds a Master of Science in Geological Oceanography from the University of South Florida. She has considerable experience managing some of the firm's largest and most complex projects.

Colin Cooper, GISP is a Technical Domain Expert for NV5 Geospatial in the fields of topographic and bathymetric lidar. He holds a Master of Science in Geography from Oregon State University.



Dewberry is a leading, market-facing firm with a proven history of providing professional services to public- and private-sector clients. Established in 1956 and headquartered in Fairfax, Virginia, Dewberry's professionals are dedicated to solving clients' most complex challenges and transforming their communities. The firm harnesses the power of geospatial science to offer complete end-to-end remote sensing and mapping services starting with state-of-the-art airborne lidar sensors to automated processing, surveying, web/mobile GIS, and advanced data analytics. Dewberry creates, analyzes, and builds geospatial data and tools, to help clients integrate, share, and simplify the use of information allowing for more effective and efficient decision making.

Dewberry's geospatial and technology services team includes more than 250 professionals who create, analyze, and build tools to share geospatial data, and help clients integrate these tools into their daily lives. By fusing multiple data sets together for more efficient data mining, Dewberry provides clients with easy-to-use tools that simplify the use of information to allow for more effective and efficient decision making.

Dewberry recently purchased two airborne lidar sensors – the RIEGL VQ-1560 IIS topographic airborne lidar sensor and the Teledyne CZMIL SuperNova, a powerful topobathymetric mapping sensor. This investment allows Dewberry to expand its mapping capabilities with current clients, keep the entire acquisition life-cycle in-house, and monitor the quality of its products. The firm is excited to empower their clients with access to the most innovative technology to meet their topographic/lidar needs, delivering hi-definition lidar datasets quickly and efficiently.

Dewberry has also implemented two initiatives to facilitate client communication and data processing efficiency. The firm is using Esri-powered, client-facing dashboards combined with quick-look technology, allowing clients to view data acquisition in near real-time and be an active partner in remote sensing activities. The second initiative focuses on improved feature extraction efficiency through automation. Dewberry's IT-team built custom multi-threaded, extended-memory computers dedicated for artificial intelligence (AI)/machine learning (ML) processing. These computers are used for feature extraction and automated classification of lidar data. This AI/ML workflow increases efficiency and decreases delivery time of geospatial products to clients.

The firm's solid performance processes in geospatial technologies and corporate IT services led to it being appraised at Level 3 of the CMMI Institute's Capability Maturity Model Integration (CMMI) in Services and Development Models. In 2021, Dewberry received industry-wide recognition, including five awards from Esri, the American Society for Photogrammetry and Remote Sensing (ASPRS), the Management Association for Private Photogrammetric Surveyors (MAPPS), and the Grand Award and the Pinnacle Award from the American Council of Engineering Companies (ACEC).

Dewberry works seamlessly to provide geospatial mapping and technology services (GTS) across various market segments. With more than 48 years of GTS experience, the firm is dedicated to understanding and applying the latest tools, trends, and technologies. Dewberry employs the latest GIS software and database platforms, including the full suite of ESRI products. The firm's products and services include application, web, and cloud-based development; system integration; database design mapping; data fusion; and mobile solutions. To learn more, visit www.dewberry.com.

Dewberry
Amar Nayegandhi
1000 North Ashley Drive, Suite 801, Tampa, FL 33602-3718
813.421.8642 | www.dewberry.com
anayegandhi@dewberry.com



Dewberry®

Need a Custom USGS Topo Map? Here is How to Make it Yourself!

INTRODUCTION

The United States Geological Survey (USGS) has over 140 years of experience in providing high-quality topographic maps in the US. In 1879, the USGS began to map the Nation's topography. This mapping was done at different levels of detail, to support various land use and other purposes. As the years passed, the USGS produced new map versions of each area. These maps were published at several scales, the most popular being the 1:24,000 scale which displayed 7.5-minute quadrangle published between 1947 – 1992.

In 2011, as a goal of the Historic Topographic Map Collection (HTMC), the USGS constructed a digital repository of USGS 1:250,000 scale and larger maps printed between 1884 and 2006. There are currently over 178,000 maps in this historic collection in addition to the current digital US Topo series. Both the HTMC and the US Topo series are available as GeoPDFs through The

National Map (<https://www.usgs.gov/programs/national-geospatial-program/national-map>) and the USGS Store (<https://store.usgs.gov/>).

But ... what if you need a topographic map for a small area, or a map for a specific app and do not want to download an entire 7.5-minute USGS quadrangle? Well... the USGS has a solution called "topoBuilder".

MAKING A CUSTOM TOPO MAP

"topoBuilder" is a USGS on-demand topo map application that can be accessed through The National Map or directly at: <https://topobuilder.nationalmap.gov>. The topoBuilder app permits the end-user to make your own topographic map, centered on your specified coordinates, in multiple formats, using the best available National Map data. The following steps demonstrate how to make a custom topo map for an area near Tallahassee, Florida starting at The National Map.

STEP 1

From "The National Map" web-viewer, select the topoBuilder app (upper right on banner)

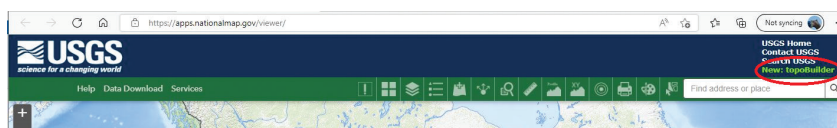


Figure 1. The topoBuilder (green) icon on the U.S. National Map.

STEP 2

That will get you to the topoBuilder app and selecting "Create an OnDemand Topo" will get you to the topoBuilder app. (You may need to read and then close any notifications.)

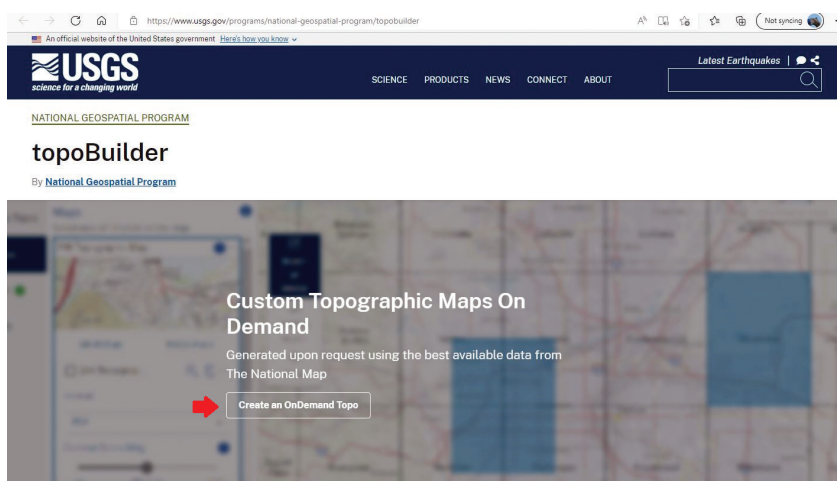


Figure 2. The topoBuilder introductory screen.

Photogrammetric Engineering & Remote Sensing
Vol. 88, No. 10, October 2022, pp. 621-624.
0099-1112/22/621-624

© 2022 American Society for Photogrammetry and Remote Sensing
doi: 10.14358/PERS.88.10.624

STEP 3

On the topoBuilder app, select the map type by clicking on the map-type you want to make (in this case there is only the 7.5-minute topo) and click “NEXT” on the bottom center:

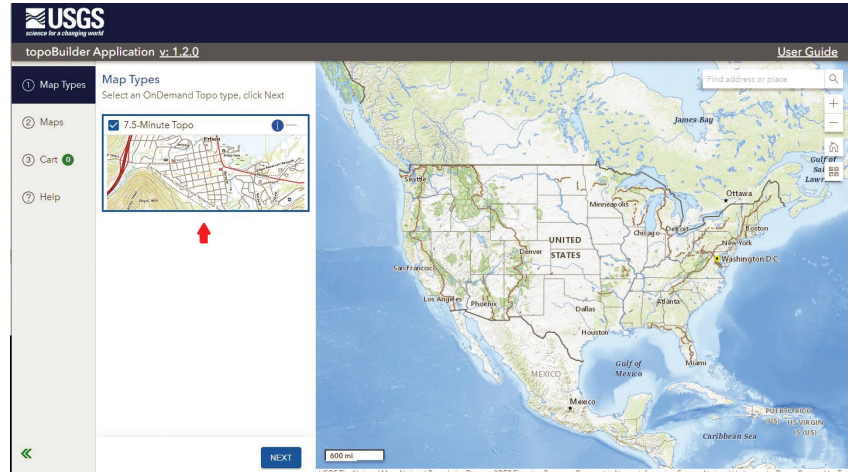


Figure 3. The topoBuilder interactive map interface.

STEP 4

Click on the “Custom Select” and using the mouse wheel, ZOOM-in to your area of interest. When you zoom-in, you will see a blue-shaded box that you can use to select a 7-minute quad area. Position the box centered on your area of interest and click the mouse (left-click) to select that area. In this case, I selected an area around Tallahassee, Florida that is centered on four x 7.5-minute quadrangles.

At this point, you can also choose your export options (PDF is the default, but you can use the dropdown to choose TIF) and choose the amount of Contour Smoothing (default is Medium) by sliding the slider.

Clicking “ADD” will put the map into your cart and go to the next step.

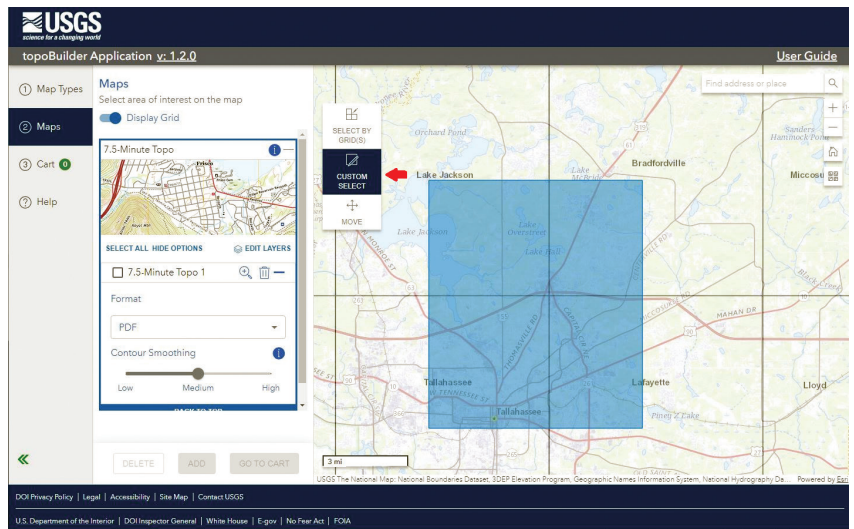


Figure 4. Selecting a custom area of interest on the topoBuilder map interface.

STEP 5

Selecting the EDIT MAPS option will let you review your choices and then pressing SAVE will save your map

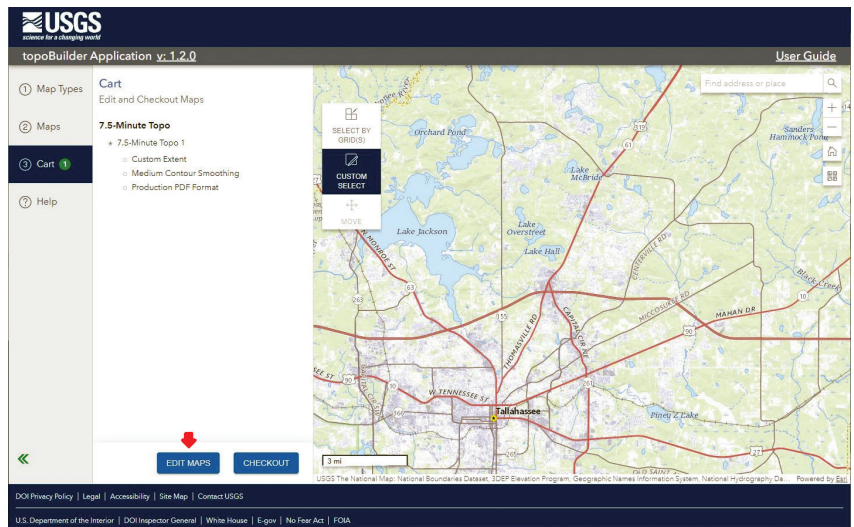


Figure 5. The Cart resulting from a custom area of interest from topoBuilder.

STEP 6

Use the CHECKOUT button to finalize your order and get to the Check Out screen where you will enter your e-mail address and press CHECKOUT (again):

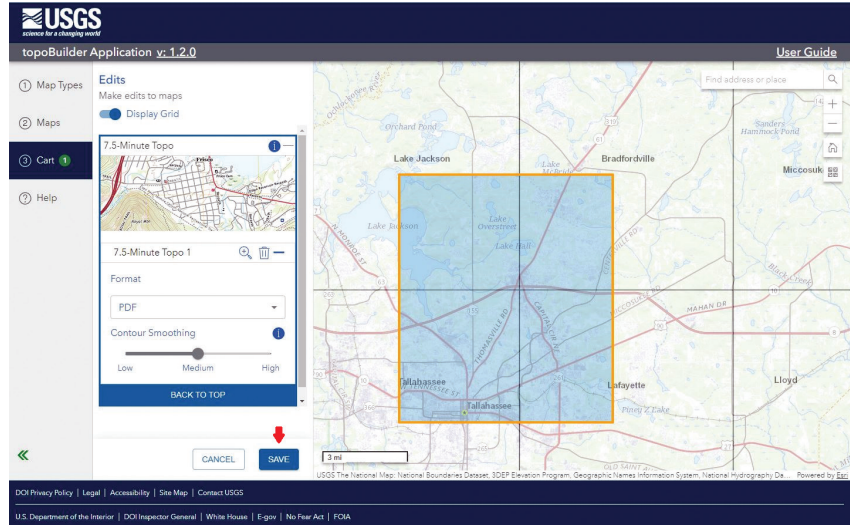


Figure 6. The confirmation and checkout screen from topoBuilder.

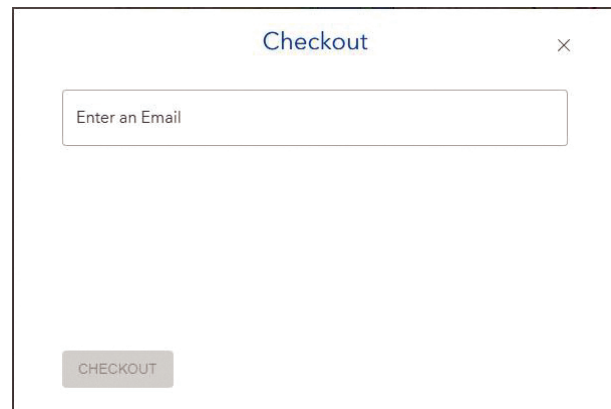


Figure 7. The Checkout Screen from topoBuilder. You need to enter your e-mail address to be used for sending the link to your quadmap. Once your e-mail address is entered, press “CHECKOUT” to complete.

The app will process your request, and after a short time, will return:

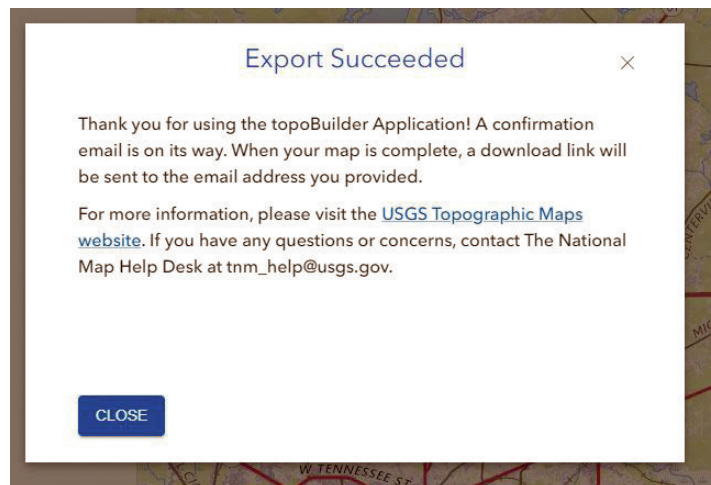


Figure 8. The Export Succeeded screen topoBuilder generates when your map has been successfully generated.

You can CLOSE this notice and you will receive an e-mail message that your map is being processed. When your map is ready, you will receive another e-mail with a link and download instructions.

Here is my finished map. Notice that there are no collars around the four 7.5-minute quadrangles that comprise my map and you can see the specific area (red rectangle) on the map collar,

Additional help is available at: <https://www.usgs.gov/programs/national-geospatial-program/topobuilder> and tnm_help@usgs.gov. Special thanks to Alexandra “Xan” Fredericks (AFredericks@USGSgov). Xan is the USGS National Map Liaison to Florida, Puerto Rico and the US Virgin Islands and demonstrated the topoBuilder application during the Spring 2022 Fl-ASPRS/UF Lidar Workshop. She is also a past president of the Florida Region – ASPRS.

Send your questions, comments, and tips to GISTT@ASPRS.org.

Al Karlin, Ph.D., CMS-L, GISP is with Dewberry’s Geospatial and Technology Services group in Tampa, FL. As a senior geospatial scientist, Al works with all aspects of Lidar, remote sensing, photogrammetry, and GIS-related projects. He also teaches beginning map making at the University of Tampa.



Figure 9. The final topoBuilder map for the area of interest. Note (1) the area of interest is shown in the red box on the map collar, and (2) that the collars of the four USGS quadmaps have been removed to make a single mosaic.

Available on the ASPRS Website



The 4th Edition of the Manual of Remote Sensing!

The *Manual of Remote Sensing, 4th Ed.* (MRS-4) is an “enhanced” electronic publication available online from ASPRS. This edition expands its scope from previous editions, focusing on new and updated material since the turn of the 21st Century. Stanley Morain (Editor-in-Chief), and co-editors Michael Renslow and Amelia Budge have compiled material provided by numerous contributors who are experts in various aspects of remote sensing technologies, data preservation practices, data access mechanisms, data processing and modeling techniques, societal benefits, and legal aspects such as space policies and space law. These topics are organized into nine chapters. MRS4 is unique from previous editions in that it is a “living” document that can be updated easily in years to come as new technologies and practices evolve. It also is designed to include animated illustrations and videos to further enhance the reader’s experience.

MRS-4 is available to ASPRS Members as a member benefit or can be purchased by non-members. To access MRS-4, visit <https://my.asprs.org/mrs4>.



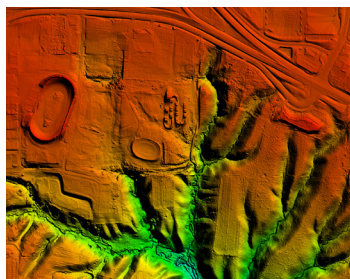
SURDEX CORPORATION: YOUR STRATEGIC GEOSPATIAL RESOURCE

Surdex Corporation is a full-service photogrammetric mapping firm in St. Louis, Missouri, that has served public and private sectors for over 65 years. Our focus is to consistently deliver premium quality geospatial products. Our extensive acquisition and processing resources provide a significant production capacity, ensuring we have the ability to meet your schedule without compromising quality. Our experience, communications and production procedures ensure every project is given a custom design and executed in a manner that will meet all project specifications – *first time right, on time.*



Our services include:

- Aerial imagery and lidar acquisition
- Lidar processing
- Digital orthoimagery production
- Planimetric mapping
- Topographic mapping
- Disaster mapping



We serve a wide range of both public and private sector clients:

- Municipal, county, state and federal government entities (including DOTs)
- Surveyors
- Engineering and construction firms
- Energy firms (oil and gas, solar, and wind)

Surdex's aircraft, supported by in-house maintenance personnel, and sensors are key to successfully completing numerous simultaneous projects across the country. Our acquisition assets include:

- A fleet of 10 Cessna aircraft
- 9 digital image sensors – 5 Leica ADS100s and 4 DMC-1s
- 3 lidar sensors – 2 Galaxy T2000s and 1 Galaxy Prime

We maintain a staff of approximately 100 employees including many with degrees in mapping or engineering fields. Our staff includes 8 ASPRS Certified Photogrammetrists, 1 ASPRS CMS-Lidar, 1 ASPRS CMT-GIS, 1 GISP certification, 2 Registered Land Surveyors and 1 Project Management Professional (PMP) certification. This depth of skilled professionals enables us to carefully design a custom plan for each project, to avoid issues and to mitigate them if they do occur.

In addition to completing numerous county/municipal government projects annually, Surdex is a prime contractor on several national multi-year programs such as the USDA PINE and the USGS GPSC4 program, and we have an IDIQ contract with the US Army Corps of Engineers for Surveying and Mapping. We also have a GSA contract for Earth Observation Solutions and numerous state DOT contracts.



Surdex routinely undertakes projects ranging in size from a single development site to an entire state. Our production capacity and project management enable us to manage numerous concurrent projects – and to deliver a quality product that meets each project's specifications and schedule. We institute redundant quality control processes and inspections at every major production phase, assuring that no work proceeds to the next step until it is validated against project standards. Consequently, Surdex's products live up to our clients' expectations for quality and accuracy.

If receiving a quality product in a timely manner is important to you, call Surdex to see how we can help.

Surdex Corporation
520 Spirit of St. Louis Boulevard
Chesterfield, MO 63005
(636) 368-4400 | www.surdex.com



STAND OUT FROM THE REST

EARN ASPRS CERTIFICATION

ASPRS congratulates these recently Certified and Re-certified individuals:

RECERTIFIED PHOTOGRAMMETRIST

Charles E. Meyers, Certification #R1329CP

Effective May 23, 2022, expires May 23, 2027

Bryan O'Malley, Certification #R1326CP

Effective May 2, 2022, expires May 2, 2027

Edward Rodrigue, Certification #R968CP

Effective April 3, 2022, expires April 3, 2027

Jason Dolf, Certification #R1488CP

Effective April 19, 2021, expires April 19, 2026

Matthew Doty, Certification #R1580CP

Effective March 16, 2020, expires March 16, 2025

Craig Fry, Certification #R1336CP

Effective October 7, 2022, expires 7, 2027

RECERTIFIED LIDAR TECHNOLOGIST

Matthew Doty, Certification #R043LT

Effective May 13, 2022, expires May 13, 2025

RECERTIFIED MAPPING SCIENTIST GIS/LIS

William M. Stiteler, Certification #R190GS

Effective April 11, 2022, expires April 11, 2027

RECERTIFIED REMOTE SENSING TECHNOLOGIST

Kevin F. May, Certification #R202RST

Effective March 12, 2021, expires March 12, 2024

RECERTIFIED MAPPING SCIENTIST – REMOTE SENSING

William M. Stiteler, Certification #R154RS

Effective April 4, 2022, expires April 4, 2027

CERTIFIED MAPPING SCIENTIST GIS/LIS

Wesley Street, Certification #GS268

Effective July 13, 2022, expires July 13, 2027

Hurmain Ariffin, Certification #GS312

Effective July 29, 2022, Expires July 29, 2027

ASPRS Certification validates your professional practice and experience. It differentiates you from others in the profession. For more information on the ASPRS Certification program: contact certification@asprs.org, visit <https://www.asprs.org/general/asprs-certification-program.html>.



**Too young to drive the car? Perhaps!
But not too young to be curious about geospatial sciences.**

The ASPRS Foundation was established to advance the understanding and use of spatial data for the betterment of humankind. The Foundation provides grants, scholarships, loans and other forms of aid to individuals or organizations pursuing knowledge of imaging and geospatial information science and technology, and their applications across the scientific, governmental, and commercial sectors.

Support the Foundation, because when he is ready so will we.

asprsfoundation.org/donate



Ad Index

| | | | | |
|--------------------|--|--|--|-----|
| Dewberry | | www.dewberry.com | | 620 |
| Surdex Corporation | | www.surdex.com | | 625 |



& GRIDS & DATUMS

GRENADA

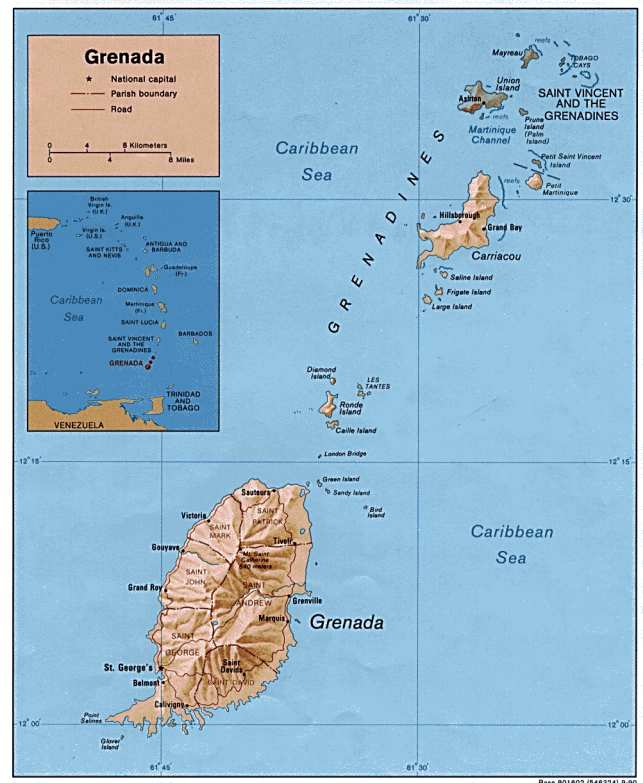
BY Clifford J. Mugnier, CP, CMS, FASPRS

The Grids & Datums column has completed an exploration of every country on the Earth. For those who did not get to enjoy this world tour the first time, *PE&RS* is reprinting prior articles from the column. This month's article on Grenada was originally printed in 2005 but contains updates to their coordinate system since then.

Discovered by Christopher Columbus in 1498 on his third voyage, the island was not settled until 1609 when the English attempted to establish tobacco plantations. Native Carib Indians made numerous raids on the English settlers and convinced them to abandon the island. In 1650, the governor of Martinique purchased Grenada from the Caribs, and resettled the island with about 200 French citizens. After a year of subsequent raids by the Caribs, a contingent of French soldiers was sent to Grenada to secure the island. The Caribs were routed at Sauteurs Bay, but rather than surrender, the entire Carib population leaped to their deaths from the island cliffs. Thanks to *Lonely Planet* 2004: "The French then set about establishing plantations of indigo, tobacco, coffee, cocoa and sugar, which were worked by African slaves. Grenada remained under French control until captured by the British in 1762.

Over the next two decades it teetered between the two colonial powers until it was ceded to the Brits in 1783. It remained under British rule until independence, though animosity lingered between the British colonialists and the minority French settlers, with violence erupting periodically. In 1877, Grenada became a Crown Colony. In 1967, Grenada became an associate state within the British Commonwealth. Grenada and the neighboring Grenadine Islands of Carriacou and Petit Martinique adopted a constitution in 1973 and became an independent nation in 1974."

Dubbed the "Spice Island" because of its impressive production of nutmeg, mace, cinnamon, ginger, and cloves, Grenada has a rugged mountainous interior of rainforests and waterfalls and an indented coastline with protected bays



and secluded beaches. Grenada is comprised of the islands of Grenada, Carriacou, and Petit Martinique. Located just north of Trinidad and Tobago (*PE&RS*, November 2000), and just south of St. Vincent (*PE&RS*, February 2004), the area of Grenada (340 km²), is twice the size of Washington, D.C. With a coastline of 121 km, the terrain is volcanic in origin with central mountains. The lowest point is the Caribbean Sea, and the highest point is Mount Saint Catherine (840 m).

The British Directorate of Colonial Surveys (DCS) flew the first aerial photography of Grenada in 1951. The original geodetic surveys of the island were performed by DCS in 1953, and the origin point is the astronomical station GS 8,

Photogrammetric Engineering & Remote Sensing
Vol. 88, No. 10, October 2022, pp. 627-628.
0099-1112/22/627-628

© 2022 American Society for Photogrammetry
and Remote Sensing
doi: 10.14358/PERS.88.10.627

Santa Maria (at the Santa Maria Hotel yard), where: $\Phi_0 = 12^\circ 02' 36.56''$ N and $\Lambda_0 = 61^\circ 45' 12.495''$ West of Greenwich. The defining azimuth to G5 North Extension is $\alpha_0 = 207^\circ 30' 46.55''$ East of North, and scale is defined by the length from G1 West Base (Grand Anse Rum Distillery Hill) to G2 East Base (SE of the Grand Anse Rum Distillery chimneys) of 1991.394 meters. The height of Santa Maria (H_0) = 160.24 feet, determined by leveling from the Colony bench mark at St. Georges Harbor which is 3.17 feet above mean sea level. The ellipsoid of reference is the Clarke 1880 where: $a = 6,378,249.145$ m, $1/f = 293.465$. The grid system used for Grenada is the BWI Transverse Mercator Grid where the central meridian, $\lambda_0 = 62^\circ$ W, the latitude of origin $\phi_0 =$ equator, the scale factor at the latitude of origin $m_0 = 0.9995$, False Easting = 400 km, and False Northing = nil. The formulae are the Gauss-Krüger, but for such a small span of latitude and longitude that includes all three islands; the distinction in this case is irrelevant. As is common with the BWI Grid usage, the grid is used as an “atlas index” numbering system for the popular tourist maps, and is not numbered with coordinate values but with an alphanumeric system for facile use to locate tourist interest points. The grid is easy to recover if one is familiar with the standard BWI grid conventions, but the defining parameters are unfortunately obscure to many.

“In Grenada, four Navy A-7 Corsair aircraft strafed a U.S. Army command post, inflicting 17 American casualties (Doton, *Acquisition Quarterly Review*, 1996). That tragedy highlighted the Services’ failure to establish a common positional picture. Each Service brought its own maps and map systems to the fight. The ground forces were unable to accurately describe a point on the ground to the supporting pilots. Air, ground, and sea Services planned and operated using separate maps referenced to three distinctly different coordinate systems. Accustomed to large-scale maps depicting terrain in familiar grids, Army units deploying from Fort Bragg used maps constructed by the Army’s 100th Engineer Company (Cartographic), from a tourist map with an arbitrary grid overlay. Despite pictures of palm trees in the margins, the map was excellent. Constructed by British military engineers, the base map included highly accurate survey data replete with topographic contours. The American Army engineers merely added black grid lines for ground troops to use as a grid reference system. While this worked well for the Army, coordinates from the gridded overlay were useless to any combatant without a copy of the modified tourist map. Some historians link the strafing of the U.S. Army command post to this lack of a common positional picture.

“Ground units experienced difficulty in orienting themselves and in directing supporting gunfire and airstrikes. [This] inadvertent airstrike...has been blamed partly on this chart confusion problem” (Rivard, *DTIC* 1985). The failure to create a common reference for planning highlighted the Services’ utter lack of attention to planning the joint fight. The ‘tourist map’ debacle merited considerable media atten-

tion, providing further grist for 1986 Goldwater-Nichols Act proponents.” (Gruetzmacher, Holtery, and Putney, Joint Forces Staff College Joint and Combined Staff Officer School, #02-02, 2002). A GPS survey by the U.S. National Geodetic Survey (NGS) occupied the station GS 15, Fort Frederick in 1996. I computed a singlepoint datum shift relation from Grenada 1953 Datum to WGS 84 Datum as: $\Delta X = +72$ m, $\Delta Y = +213$ m, and $\Delta Z = +93$ m. Thanks to Dennis McCleary of NGA for validation that the Santa Maria “astro” position was the same as the geodetic position I received from Dave Doyle of NGS.

UNAVCO installs COCONet cGPS site CN46 in Carriacou, Grenada

Determining how the Caribbean plate moves with respect to the neighboring North America and South America plates has been a major challenge. Geologic plate motion models using seafloor magnetic anomaly rates, transform fault azimuths, and slip vectors are challenging due to sparse data. The only rates come from the Cayman Spreading Center, and seismicity at the eastern boundary is low due to slow convergence. Moreover, the boundary geometry is still unclear, since the Caribbean plate’s north and south boundaries are complex deformation zones.

GPS data continue to provide key clues to the Caribbean region’s geologic faults. GPS stations are currently being installed as part of the Continuously Operating Caribbean GPS Observational Network (COCONet), strengthening the indispensable collection of data belonging to a region that faces many atmospheric and geologic natural hazards.

While most people in the Caribbean were enjoying their time off for Easter weekend, UNAVCO engineers Jacob Sklar and Michael Fend were installing COCONet GPS site CN46 on Carriacou Island, Grenada April 16 - 24, 2014. Carriacou Island, not to be confused with Curacao, is a two-hour ferry ride north of Grenada. UNAVCO worked closely with Terence Walters of Grenada’s National Disaster Management Agency (NaDMA) and Stephen George from the University of the West Indies Seismic Research Centre (UWI). CN46 is co-located with UWI’s seismic vault; GPS, meteorological, and seismic data are all being transmitted via a satellite connection. Collaborating with UWI will allow both UNAVCO and UWI personnel to monitor the health of the site.

<https://www.unavco.org/highlights/2014/carriacou.html>.

The contents of this column reflect the views of the author, who is responsible for the facts and accuracy of the data presented herein. The contents do not necessarily reflect the official views or policies of the American Society for Photogrammetry and Remote Sensing and/or the Louisiana State University Center for GeoInformatics (C⁴G).

This column was previously published in *PE&RS*.

JOURNAL STAFF

Editor-In-Chief

Alper Yilmaz, Ph.D., PERSeditor@asprs.org

Associate Editors

Valérie Gouet-Brunet, Ph.D., valerie.gouet@ign.fr
Petra Helmholz, Ph.D., Petra.Helmholz@curtin.edu.au
Dorota Iwaszczuk, Ph.D., dorota.iwaszczuk@tum.de
Desheng Liu, Ph.D., liu.738@osu.edu
Clement Mallet, Ph.D., clemallet@gmail.com
Sidike Paheding, Ph.D., spahedin@mtu.edu
Norbert Pfeifer, np@ipf.tuwien.ac.at
Rongjun Qin, Ph.D., qin.324@osu.edu
Ribana Roscher, Ph.D., ribana.roscher@uni-bonn.de
Zhenfeng Shao, Ph.D., shaozhenfeng@whu.edu.cn
Filiz Sunar, Ph.D., fsunar@itu.edu.tr
Prasad Thenkabail, Ph.D., pthenkabail@usgs.gov
Dongdong Wang, Ph.D., ddwang@umd.edu
Qunming Wang, Ph.D., wqm11111@126.com
Ruisheng Wang, Ph.D., ruiswang@ucalgary.ca
Jan Dirk Wegner, jan.wegner@geod.baug.ethz.ch
Bo Wu, Ph.D., bo.wu@polyu.edu.hk
Michael Yang, Ph.D., michael.yang@utwente.nl
Hongyan Zhang, zhanghongyan@whu.edu.cn

Contributing Editors

Highlight Editor

Jie Shan, Ph.D., jshan@ecn.purdue.edu

Feature Articles

Michael Joos, CP, GISP, featureeditor@asprs.org

Grids & Datums Column

Clifford J. Mugnier, C.P., C.M.S., cjmce@lsu.edu

Book Reviews

Sagar Deshpande, Ph.D., bookreview@asprs.org

Mapping Matters Column

Qassim Abdullah, Ph.D., Mapping_Matters@asprs.org

GIS Tips & Tricks

Alvan Karlin, Ph.D., CMS-L, GISP akarlin@Dewberry.com

SectorInsight

Youssef Kaddoura, Ph.D., kaddoura@ufl.edu
Bob Ryerson, Ph.D., FASPRS, bryerson@kimgeomatics.com
Hamdy Elsayed, Hamdy.Elsayed@teledyne.com

ASPRS Staff

Assistant Director — Publications

Rae Kelley, rkelley@asprs.org

Electronic Publications Manager/Graphic Artist

Matthew Austin, maustin@asprs.org

Advertising Sales Representative

Bill Spilman, bill@innovativemediasolutions.com

ASPRS ESTES TEACHING EXCELLENCE AWARD: CALL FOR NOMINATIONS

We are seeking nominations for the American Society for Photogrammetry and Remote Sensing (ASPRS).

Estes Teaching award. The Estes Memorial Teaching Award is named in honor of Professor John E. ("Jack") Estes, teacher, mentor, scientist, and friend of ASPRS. The Estes award recognizes individual contributions to higher education in remote sensing and geographic information systems technology with a particular focus on teaching excellence. The Award consists of a presentation plaque and a cash award of \$3000 and is presented by ASPRS through the ASPRS Foundation.

Nominations should present evidence for superior teaching, which includes course, curricular and program development, testimonials from supervisors and former students, teaching awards and demonstrated student success.

The nomination materials should include:

- i. Letter of nomination.
- ii. A Curriculum Vitae.
- iii. Evidence highlighting achievement in teaching excellence.
- iv. Two letters of recommendation highlighting teaching excellence.

Eligibility to receive the Award is not restricted to members of ASPRS. The Award is made to an individual (or two or more collaborating individuals, provide each played a major role in the achievement) who best meets the criteria established. The Award is not made to companies, agencies, bureaus, schools, or associations; however, their personnel are eligible as individuals to receive the Award.

Please email the nomination materials as a single PDF file to awards@asprs.org. Nominations are due by 15 November, 2022

NEW ASPRS MEMBERS

ASPRS would like to welcome the following new members!

Claudia Elisa Aviles Toledo

John Burgin

Tim Burkholder

Carlos Andres Castillo

Christopher R. Dolly

Nima Esmaeilzadeh

Emily D. Graham, GISP

Kyle Ince

Suraj K C

Jekope Kalinisei

Holly Knox

Michael James Lalla

Vanessa Self Miller

Maria Oreshkina

Julie Patterson

Megan R. Perron

Karoll Quijano

Kjell Ryerson

Joseph Sandy Samberg

Gustavo Serrato

Prof. Daniel Sousa

Dr. Christopher Gayle Tate

FOR MORE INFORMATION ON ASPRS MEMBERSHIP, VISIT

[HTTP://WWW.ASPRS.ORG/JOIN-NOW](http://www.asprs.org/join-now)

Call for *PE&RS* Special Issue Submissions

Innovative Methods for Geospatial Data using Remote Sensing and GIS

Internationally comparable data is a global need for managing resources, monitoring current trends and taking actions for sustainable living. Even though there has been a significant progress on geospatial data availability, extensive data gaps are still a major problem for general assessment and supervise the progress through the years. According to United Nations 2022 The Sustainable Development Goals Report, while health and energy sectors have the highest data available, limited data available for climate action.

The COVID-19 crisis has also shown that there are innovative data collection methods utilizing information and computer technologies. However, only 5% of the countries have benefit from remote sensing technologies to measure the impact of COVID-19. Additionally, novel approaches such as artificial intelligence should be used in conjunction with assessments to make sure they are put to use for critical situations.

The recent developments in remote sensing, geographic information systems and ICT have provided a wide accessibility to create geospatial data for various purposes. The proposed special issue focuses on *“Innovative Methods for Geospatial Data using Remote Sensing and GIS”* for wide range of applications. This special issue aims to bring researchers to share knowledge and their expertise about innovative methods to contribute to fill data gaps around the world for a better future.

The proposed special issue aims to contributes ASPRS’s key mission on ‘Simplify and promote the use of image-based geospatial technologies for the end-user’, ‘Promote collaboration between end users and geospatial experts to match data and technology to applications and solutions’ and ‘promote the transfer of geospatial data and information technology to developing nations’ by providing innovative methods to create geospatial data using remote sensing and geographic information systems utilizing state-of-the-art developments and solutions.

Deadline for Manuscript Submission—July 1, 2023

Submit your Manuscript to <http://asprs-pers.edmgr.com>

Guest Editors

Dr. Tolga Bakirman, bakirman@yildiz.edu.tr , *Yildiz Technical University, Department of Geomatic Engineering, Davutpasa Campus, 34220 Esenler-Istanbul/Turkey*

Dr. George Arampatzis, garampatzis@pem.tuc.gr, *Technical University Crete, School of Production Engineering & Management, 73100 Chania – Crete/Greece*

A Novel Residual Attitude Estimation Approach Using Georeferenced Satellite Imagery

Bhaskar Dubey and B. Kartikeyan

Abstract

This article presents an efficient novel approach estimating residual attitude based on geometrically corrected (GEO) satellite images. A technique is presented that uses orbital plane geometry to compute the rotation angle as a function of geographic latitude between GEO image space and radiometrically corrected (RAD) image space. First, a nonlinear forward model is established that translates the residual errors in roll, pitch, and yaw to scan errors and pixel errors in GEO image space. Subsequently, the inverse problem is solved using Newton's method of nonlinear optimization for estimating residual roll, pitch, and yaw. We demonstrate our results on data products of the high-resolution Indian satellites Cartosat-2E and Cartosat-2F. Further, the superiority of the proposed method is established by comparing it with multiple existing methods in the literature. The R^2 measures of goodness of fit for roll, pitch, and yaw estimation based on RAD and GEO products using the proposed method are 0.65, 0.99, and 0.65, respectively; using the existing method, they are 0.074, 0.005, and 0.50.

Introduction

Attitude measurement of a satellite is carried out by the onboard sensors, namely gyroscopes, magnetometers, and star sensors, which are part of the satellite's attitude and orbit control system. Vast literature is available on precise real-time satellite attitude determination and calibration (see, e.g., Grassi 1997; Crassidis *et al.* 2007; Soken *et al.* 2014; Pan *et al.* 2016; Yang *et al.* 2021; and the references therein). Often, there exists residual error in attitude estimation, which is compensated via ground-based calibration with the help of precise ground control points (GCPs; Davison 1986; Radhadevi *et al.* 2011; Chen *et al.* 2017).

The problem of estimating residual attitude of a remote sensing satellite is one of the fundamental interests in accurate georeferencing and geometric calibration (Ford and Zanelli 1985; Tommaselli and Tozzi 1996; Srivastava and Alurkar 1997). Georeferencing is carried out using a physical sensor model that relies on the knowledge of orbit and orientation parameters, both exterior and interior, and digital elevation models (DEMs; Westin 1992; Jiang *et al.* 2022). The geometric rectification can also be carried out through other methods—for instance, rational function model-based methods (Xiong and Zhang 2009; Shen *et al.* 2017; Dubey *et al.* 2019) and equivalent geometric sensor model-based methods (Cao *et al.* 2019). Often, system level geometrically corrected (GEO) products (basic GEO products based on system knowledge alone) have high location errors for various reasons, namely orbit and attitude errors, micro-vibrations of the platform, terrain undulations, and errors in interior orientation parameters. In recent Indian Remote Sensing (IRS) missions, the system-level location error is on the order of 100 to 200 m (Srinivasan *et al.* 2008). A major part of this error is attributed to error in the measurement of satellite attitude by the onboard sensors. Thus, the precise estimation of residual attitude is very important for improving system-level location accuracy, and also for generating more accurate final products. A rigorous in-flight geometric calibration, which also involves compensation for residual

attitude biases, is carried out in order to improve the geometric accuracies and overall system-level location errors (Leprince *et al.* 2007; Radhadevi and Solanki 2008; Zhang *et al.* 2014; Wang *et al.* 2017).

In the literature, residual attitude estimation has been explored by various authors in various ways (e.g., Mahapatra *et al.* 2004; Pulsule *et al.* 2008; Weser *et al.* 2008; Dubey and Kartikeyan 2018). Wahba (1965) aimed to find a best-approximating residual orthogonal matrix to minimize the location errors at a few conspicuous points. Mahapatra *et al.* (2004) forged discussions for computing residual attitude based on Taylor-series linearization of the collinearity equations. We (Dubey and Kartikeya 2018) recently established an improved approach for estimating residual attitude based on radiometrically corrected (RAD) products, wherein we directly model the effect of residual roll, pitch, and yaw in terms of scan errors and pixel errors at a few GCPs in RAD image space. Due to this, that approach becomes advantageous in many situations over other methods, especially when a user does not have orbit, attitude, and sensor-model parameters to perform full-fledged geometric calibration for estimating residual attitude biases. The approach is also highly suitable to a data quality evaluation system where the end products are validated for quality norms, namely location errors, targeting errors, internal distortion, and residual attitude, and necessary feedback is provided to concerned data-product generation and mission operations teams.

In this article, our aim is to extend those previous results to GEO products, as these are level 2 products which are frequently demanded by geospatial data users. The image space in GEO products is often rotated with a certain angle based on satellite heading angle and imaging area latitude with respect to the RAD image space, apart from different scales and other terrain-related local distortions. Due to these shortcomings, our previous procedure (Dubey and Kartikeyan (2018), which is valid only for RAD (level 1) products, cannot be applied for residual attitude estimation with GEO products. In this approach, first a conversion of image coordinates from GEO to RAD space is desired, which essentially requires a rotation matrix. The rotation matrix as a function of latitude is derived using the orbital plane geometry and analysis of the ground trace of the satellite. Subsequently, the forward and inverse models are developed for estimating residual attitude using GEO products.

The organization of the paper is as follows: in the next section, we briefly review the results for residual attitude estimation using RAD products that are extended in this article. The following section presents a methodology for estimating residual attitude using GEO products, including a method for estimating rotation angle that is required to conform the GEO image space to the RAD image space. In the section after that, experimental results using Cartosat-2S GEO data products are presented, as are several comparisons with existing results (Pulsule *et al.* 2008; Dubey and Kartikeyan 2018). Finally, we conclude the article.

Review of Residual Attitude Estimation Based on RAD Products

We previously explained in detail the process of residual attitude estimation based on radiometrically corrected products (Dubey and

Bhaskar Dubey and B. Kartikeyan are with the Image Analysis and Quality Evaluation Division of the Signal and Image Processing Group, Space Applications Centre, Indian Space Research Organisation, Ahmedabad, India (bhaskard@sac.isro.gov.in).

Contributed by Hongyan Zhang, December 1, 2021 (sent for review April 8, 2022; reviewed by Mohammed Ahmed Aldalgawy, Zhaojin Li).

Photogrammetric Engineering & Remote Sensing
Vol. 88, No. 10, October 2022, pp. 631–641.
0099-1112/22/631-641

© 2022 American Society for Photogrammetry
and Remote Sensing
doi: 10.14358/PERS.21-00095R2

**PEER-REVIEWED CONTENT
IS ONLY AVAILABLE TO
ASPRS MEMBERS AND SUBSCRIBERS**

**FOR MORE INFORMATION VISIT
[MY.ASPRS.ORG](https://my.asprs.org)**

**PEER-REVIEWED CONTENT
IS ONLY AVAILABLE TO
ASPRS MEMBERS AND SUBSCRIBERS**

**FOR MORE INFORMATION VISIT
MY.ASPRS.ORG**

**PEER-REVIEWED CONTENT
IS ONLY AVAILABLE TO
ASPRS MEMBERS AND SUBSCRIBERS**

**FOR MORE INFORMATION VISIT
[MY.ASPRS.ORG](https://my.asprs.org)**

**PEER-REVIEWED CONTENT
IS ONLY AVAILABLE TO
ASPRS MEMBERS AND SUBSCRIBERS**

**FOR MORE INFORMATION VISIT
MY.ASPRS.ORG**

**PEER-REVIEWED CONTENT
IS ONLY AVAILABLE TO
ASPRS MEMBERS AND SUBSCRIBERS**

**FOR MORE INFORMATION VISIT
[MY.ASPRS.ORG](https://my.asprs.org)**

**PEER-REVIEWED CONTENT
IS ONLY AVAILABLE TO
ASPRS MEMBERS AND SUBSCRIBERS**

**FOR MORE INFORMATION VISIT
MY.ASPRS.ORG**

**PEER-REVIEWED CONTENT
IS ONLY AVAILABLE TO
ASPRS MEMBERS AND SUBSCRIBERS**

**FOR MORE INFORMATION VISIT
[MY.ASPRS.ORG](https://my.asprs.org)**

**PEER-REVIEWED CONTENT
IS ONLY AVAILABLE TO
ASPRS MEMBERS AND SUBSCRIBERS**

**FOR MORE INFORMATION VISIT
[MY.ASPRS.ORG](https://my.asprs.org)**

**PEER-REVIEWED CONTENT
IS ONLY AVAILABLE TO
ASPRS MEMBERS AND SUBSCRIBERS**

**FOR MORE INFORMATION VISIT
MY.ASPRS.ORG**

**PEER-REVIEWED CONTENT
IS ONLY AVAILABLE TO
ASPRS MEMBERS AND SUBSCRIBERS**

**FOR MORE INFORMATION VISIT
MY.ASPRS.ORG**



Statement of Ownership, Management, and Circulation
(All Periodicals Publications Except Requester Publications)

1. Publication Title: Photogrammetric Engineering & Remote Sensing
 2. Publication Number: 0 4 3 0 - 9 6 0
 3. Filing Date: October 2022
 4. Issue Frequency: Monthly
 5. Number of Issues Published Annually: 12
 6. Annual Subscription Price: \$1105.00
 7. Complete Mailing Address of Known Office of Publication (Not printer) (Street, city, county, state, and ZIP+4®):
 ASPRS
 425 Barlow Place, Suite 210
 Bethesda, MD 20814
 Contact Person: Rae Kelley
 Telephone (include area code): 301-493-0290
 8. Complete Mailing Address of Headquarters or General Business Office of Publisher (Not printer):
 Same as block #7
 9. Full Names and Complete Mailing Addresses of Publisher, Editor, and Managing Editor (Do not leave blank):
 Publisher (Name and complete mailing address):
 ASPRS
 425 Barlow Place, Suite 201
 Bethesda, MD 20814
 Editor (Name and complete mailing address):
 Dr. Alper Yilmaz
 470 Hitchcock Hall
 Columbus, OH 43035
 Managing Editor (Name and complete mailing address):
 Rae Kelley, ASPRS
 425 Barlow Place, Suite 201
 Bethesda, MD 20814
 10. Owner (Do not leave blank. If the publication is owned by a corporation, give the name and address of the corporation immediately followed by the names and addresses of all stockholders owning or holding 1 percent or more of the total amount of stock. If not owned by a corporation, give the names and addresses of the individual owners. If owned by a partnership or other unincorporated firm, give its name and address as well as those of each individual owner. If the publication is published by a nonprofit organization, give its name and address.)
 Full Name: American Society for Photogrammetry and Remote Sensing
 Complete Mailing Address: Same as block #7
 11. Known Bondholders, Mortgagees, and Other Security Holders Owning or Holding 1 Percent or More of Total Amount of Bonds, Mortgages, or Other Securities. If none, check box None
 Full Name: Complete Mailing Address:
 12. Tax Status (For completion by nonprofit organizations authorized to mail at nonprofit rates) (Check one)
 The purpose, function, and nonprofit status of this organization and the exempt status for federal income tax purposes:
 Has Not Changed During Preceding 12 Months
 Has Changed During Preceding 12 Months (Publisher must submit explanation of change with this statement)
 PS Form 3526, July 2014 (Page 1 of 4 (see instructions page 4)) PSN: 7530-01-000-9931 PRIVACY NOTICE: See our privacy policy on www.usps.com

| 13. Publication Title | | 14. Issue Date for Circulation Data Below | |
|---|--|--|---|
| Photogrammetric Engineering & Remote Sensing | | October 2022 | |
| 15. Extent and Nature of Circulation | | Average No. Copies Each Issue During Preceding 12 Months | No. Copies of Single Issue Published Nearest to Filing Date |
| a. Total Number of Copies (Net press run) | | 350 | 303 |
| b. Paid Circulation (By Mail and Outside the Mail) | (1) Mailed Outside-County Paid Subscriptions Stated on PS Form 3541 (Include paid distribution above nominal rate, advertiser's proof copies, and exchange copies) | 152 | 150 |
| | (2) Mailed In-County Paid Subscriptions Stated on PS Form 3541 (Include paid distribution above nominal rate, advertiser's proof copies, and exchange copies) | 0 | 0 |
| | (3) Paid Distribution Outside the Mails Including Sales Through Dealers and Carriers, Street Vendors, Counter Sales, and Other Paid Distribution Outside USPS® | 63 | 0 |
| | (4) Paid Distribution by Other Classes of Mail Through the USPS (e.g., First-Class Mail®) | 55 | 54 |
| c. Total Paid Distribution (Sum of 15b (1), (2), (3), and (4)) | | 270 | 204 |
| d. Free or Nominal Rate Distribution (By Mail and Outside the Mail) | (1) Free or Nominal Rate Outside-County Copies included on PS Form 3541 | 0 | 0 |
| | (2) Free or Nominal Rate In-County Copies included on PS Form 3541 | 0 | 0 |
| | (3) Free or Nominal Rate Copies Mailed at Other Classes Through the USPS (e.g., First-Class Mail) | 0 | 0 |
| | (4) Free or Nominal Rate Distribution Outside the Mail (Carriers or other means) | 15 | 15 |
| e. Total Free or Nominal Rate Distribution (Sum of 15d (1), (2), (3) and (4)) | | 15 | 15 |
| f. Total Distribution (Sum of 15c and 15e) | | 285 | 219 |
| g. Copies not Distributed (See Instructions to Publishers #4 (page #3)) | | 80 | 99 |
| h. Total (Sum of 15f and g) | | 365 | 318 |
| i. Percent Paid (15c divided by 15f times 100) | | 94.73 | 93.15 |

* If you are claiming electronic copies, go to line 16 on page 3. If you are not claiming electronic copies, skip to line 17 on page 3.

PS Form 3526, July 2014 (Page 2 of 4)



Statement of Ownership, Management, and Circulation
(All Periodicals Publications Except Requester Publications)

16. Electronic Copy Circulation

| | Average No. Copies Each Issue During Preceding 12 Months | No. Copies of Single Issue Published Nearest to Filing Date |
|---|--|---|
| a. Paid Electronic Copies | 122 | 125 |
| b. Total Paid Print Copies (Line 15c) + Paid Electronic Copies (Line 16a) | 392 | 329 |
| c. Total Print Distribution (Line 15f) + Paid Electronic Copies (Line 16a) | 407 | 344 |
| d. Percent Paid (Both Print & Electronic Copies) (16b divided by 16c x 100) | 96.31 | 95.64 |

I certify that 50% of all my distributed copies (electronic and print) are paid above a nominal price.

17. Publication of Statement of Ownership
 If the publication is a general publication, publication of this statement is required. Will be printed in the October 2022 issue of this publication. Publication not required.

18. Signature and Title of Editor, Publisher, Business Manager, or Owner
 Signature:
 Date: 9/9/2022
 I certify that all information furnished on this form is true and complete. I understand that anyone who furnishes false or misleading information on this form or who omits material or information requested on the form may be subject to criminal sanctions (including fines and imprisonment) and/or civil sanctions (including civil penalties).

PS Form 3526, July 2014 (Page 3 of 4)

PRIVACY NOTICE: See our privacy policy on www.usps.com

Efficient Building Inventory Extraction from Satellite Imagery for Megacities

Edmond Yat-Man Lo, En-Kai Lin, Velautham Daksiya, Kuo-Shih Shao, Yi-Rung Chuang, and Tso-Chien Pan

Abstract

Accurate building inventories are essential for city planning and disaster risk management. Traditionally generated via census or selected small surveys, these suffer from data quality and/or resolution. High-resolution satellite imagery with object segmentation provides an effective alternative, readily capturing large extents. This study develops a highly automated building extraction methodology for location-based building exposure data from high (0.5 m) resolution satellite stereo imagery. The development relied on Taipei test areas covering 13.5 km² before application to the megacity of Jakarta. Of the captured Taipei buildings, 48.8% are at one-to-one extraction, improving to 71.9% for larger buildings with total floor area >8000 m², and to 99% when tightly-spaced building clusters are further included. Mean absolute error in extracted footprint area is 16% for these larger buildings. The extraction parameters are tuned for Jakarta buildings using small test areas before covering Jakarta's 643 km² with over 1.247 million buildings extracted.

Introduction

The international disaster event database NatCatSERVICE (2019) reported USD \$150 billion economic loss worldwide for the year 2018, arising from 820 natural hazard events, of which Asia accounts for 50%. Reliable estimates of the potential losses need to be developed to support effective risk management of such loss events, particularly those occurring in cities/megacities with consequent large socio-economic impacts. This in turn requires accurate descriptions of the exposures along with the hazard levels faced (Grossi et al. 2005). Such exposure data typically requires spatial maps on assets (e.g., buildings and infrastructures) at risk of covering their location, size, and other characteristics such as vulnerability, as depending on the hazard faced. Exposure maps for individual building location, height, and footprint area, and spanning the entire building inventory are needed for overlaying with hazard event maps in detailed loss assessment such as for floods and earthquakes, the two largest perils by loss magnitude for Asia (NatCatSERVICE 2019). However, such data in Asia and Southeast Asia is generally poor in quality, accessibility, and availability.

A detailed estimation of building inventory traditionally uses census data, conducting of surveys, and/or manual processing of satellite/aerial images. While rich in details at an individual building level, these are often expensive and time consuming processes, implying by necessity either coarseness in spatial resolution or in overall coverage (Figueiredo and Martina 2016; Silva et al. 2015). Automatic

building footprint (BFT) extraction from high-resolution satellite and aerial imageries are attractive alternatives in terms of data availability, acquisition cost, and the ability to cover large geographical extents (De Angeli et al. 2016; Gunasekera et al. 2015). However, challenges arise from the close proximity of buildings in dense cities, the diversity of building forms, and the level of differentiation from other background objects (Li et al. 2019). Different approaches are reported (Chen et al. 2018; Gavankar and Ghosh 2018; Li et al. 2019; Ok 2013; Huang and Zhang 2012), with multi-resolution segmentation being the most widely used (Belgiu and Drăguț 2014; Im et al. 2014). More recent studies involve deep learning applied to semantic segmentation algorithms (Lu et al. 2018; Xu et al. 2018; Sun et al. 2018; Im et al. 2014), though a large scale, city-wide application has yet to be reported.

Besides BFT, building height along with spatial location are also needed for building exposure development. Use of aerial imagery and lidar from low-flying aircraft and/or UAVs for generating Digital Surface Models (DSM) and extracting BFT and height have been reported (Haithcoat et al. 2001; Sahar et al. 2010; Awrangjeb et al. 2010; Yuan 2018; Lu et al. 2018; Xu et al. 2018; Sun et al. 2018). While such imagery offers increased resolution, there are inherent difficulties in securing permission to fly over dense, urban areas. It should also be noted that global commercial technology companies, e.g., Google have developed in-house, proprietary algorithms for extracting BFTs and heights from aerial imagery. There have also been recent, major advances in computer vision, and particularly in image segmentation using Deep Learning (DL) techniques (recent reviews are given in Garcia-Garcia et al. (2017) and Minaee et al. (2021)) applied to deep neural networks (DNN) (the most popular being convolution neural networks). Applications are reported for object detection and classification in both urban and nonurban settings (e.g., Zhang and Zhang 2018; Maltezos et al. 2019; Zhang et al. 2019). The specific works for building classification in urban areas are predominantly based on images from low flying platforms such as airborne laser scanning (ALS) or lidar (Maltezos et al. 2019) or multi-view images (Yu et al. 2021). Building footprint delineation over large areas (Wei et al. 2020) and building reconstruction at Level-of-Detail 1 (LoD-1) for small areas (Zhang and Zhang 2018; Yu et al. 2021) has been reported. Most recently (Gui and Qin 2021) applied DL techniques on very high resolution multi-view satellite images (0.3 to 0.5 m ground sampling distances) and orthophotos to achieve up to LoD-2 level of building reconstruction as demonstrated for small areas (0.5 to 2.25 km²) in three cities. Optional incorporation of the public OpenStreetMap building data further enabled refinement in building orientation. Although DL techniques and DNN have exhibited excellent capability for building extraction and reconstruction, its performance is highly correlated with the size and diversity of labelled training data as appropriate for the city scene. Therefore, building footprint and height reconstruction in complex, diverse, and dense city scenes using DNN remains an active area of research with a variety of data types (e.g., ALS, lidar, multispectral), pre- and post-processing strategies (e.g., Gui and Qin 2021), footprint regularization techniques (e.g., Wei et al. 2020), and fusion of networks (e.g., Bittner et al. 2018)

Edmond Yat-Man Lo, Velautham Daksiya, and Tso-Chien Pan are with the Institute of Catastrophe Risk Management, Nanyang Technological University, Block N1, Level B1b, 50 Nanyang Ave, Singapore 639798 (cymlo@ntu.edu.sg).

Edmond Yat-Man Lo and Tso-Chien Pan are also with the School of Civil and Environmental Engineering, Nanyang Technological University, Block N1, 50 Nanyang Ave, Singapore 639798.

En-Kai Lin, Kuo-Shih Shao, and Yi-Rung Chuang are with Sinotech Engineering Consultants, Inc., No. 171, Sec 5, Nanking E. Rd., Taipei City, Taiwan.

Contributed by Zhenfeng Shao, August 23, 2021 (sent for review April 26, 2022; reviewed by Nan Yang, Min Chen).

Photogrammetric Engineering & Remote Sensing
Vol. 88, No. 10, October 2022, pp. 643–652.
0099-1112/22/643–652

© 2022 American Society for Photogrammetry
and Remote Sensing
doi: 10.14358/PERS.21-00053R2

proposed, with building footprint and height extraction at whole-city scale yet to be demonstrated. An accuracy-quantified, low-cost, highly-automated, and scalable methodology using readily available high-resolution satellite imagery for extracting location based BFTs and heights as demonstrated here for a megacity have yet to be reported.

In the work here, an efficient, scalable BFT and height extraction methodology is developed and piloted over a 27.9 km² area in Taipei, Taiwan and further applied to cover the entire megacity of Jakarta, Indonesia covering an area of 643 km². The recently developed rational polynomial coefficient (RPC) stereo processor (RSP) (Qin 2016) for DSM generation, and the commercial *eCognition* software (<http://www.ecognition.com/>) for image segmentation are applied on high (0.5 m pixel) resolution satellite stereo imagery. Over 1.247 million buildings in Jakarta are extracted. It is further shown that only a small fraction of the extracted BFT require manual adjustment, typically larger buildings as comprising less than 10% of the total building count. This represents huge cost and time savings over traditional methods.

The study areas in Taipei and Jakarta along with data used are presented in the section “Study Areas and Data”. A description of the BFT extraction methodology and performance evaluation are in sections “Building Footprint and Height Extraction” and “Performance Evaluation”. Results from the Taipei pilot area are presented in the section “Taipei Test Areas”, while the application to Jakarta presented in the section “Jakarta City”, followed by the Conclusion section.

Study Areas and Data

The Taipei 27.9 km² pilot area is located in downtown Taipei (Figure 1a), which spans various building types, including residential, commercial, and public buildings. Two test areas comprising 13.52 km² within the pilot area are used for building extraction methodology development and validation. These two test areas represented different building characteristics, with the first test area of 8.43 km² being in a newer part of the city, while the second area of 5.09 km² is in an older part. The test areas include modern, low- to high-rise buildings, and important landmarks, such as the Taipei Train Station and the supertall 101-storey Taipei 101. Parameters in the developed building extraction methodology are tuned for Jakarta’s building using Jakarta’s two test areas comprising 9.80 km² (Figure 1b), before being applied to the whole city covering 643 km². The tuning is needed due to the different building characteristics between Taipei and Jakarta. Jakarta’s test areas are chosen from Central (Pusat) Jakarta that covers a variety of residential, commercial, and public buildings, and from north (Utara) Jakarta to further cover industrial buildings. The tallest building included is the 47-storey Menara Astra.

Taipei vector data (TVD) developed by Taipei city government in 2010 is available for both Taipei test areas and served as highly accurate ground reference data for accuracy assessment. The TVD is constructed via stereo-plotting of aerial stereo photos, and is continually updated by Sinotech Engineering Consultants Inc. The data contains detailed (1/1000 scale) boundaries of surface structures including building rooftops in vector format and rooftop height values. Figure 2 (upper panels) show histograms of the 13,208 TVD buildings’ BFT areas and heights over the test areas. Only footprint areas >50 m² are considered, as Taipei government regulations deem land plots ≤67 m² as nonbuildable. The first and second test areas have 6745 and 6459 buildings, respectively, with most having BFT areas ≤2000 m².

Similar ground reference data did not exist for Jakarta. Therefore, satellite images are manually stereo-plotted to extract accurate individual building BFT and height for use as ground reference data. The accuracy of the manual extraction was confirmed by two independent polygon extractions done on a small subset of 114 buildings (BFT areas up to 4200 m²) with the mean absolute difference in extracted BFT areas being <5%. The ground reference set has 11,626 buildings with BFT areas mostly ≤2000 m² as in Taipei but with the peak shifted to smaller BFT values (Figure 2, lower panels). Most of the buildings are also lower, ≤3 stories.

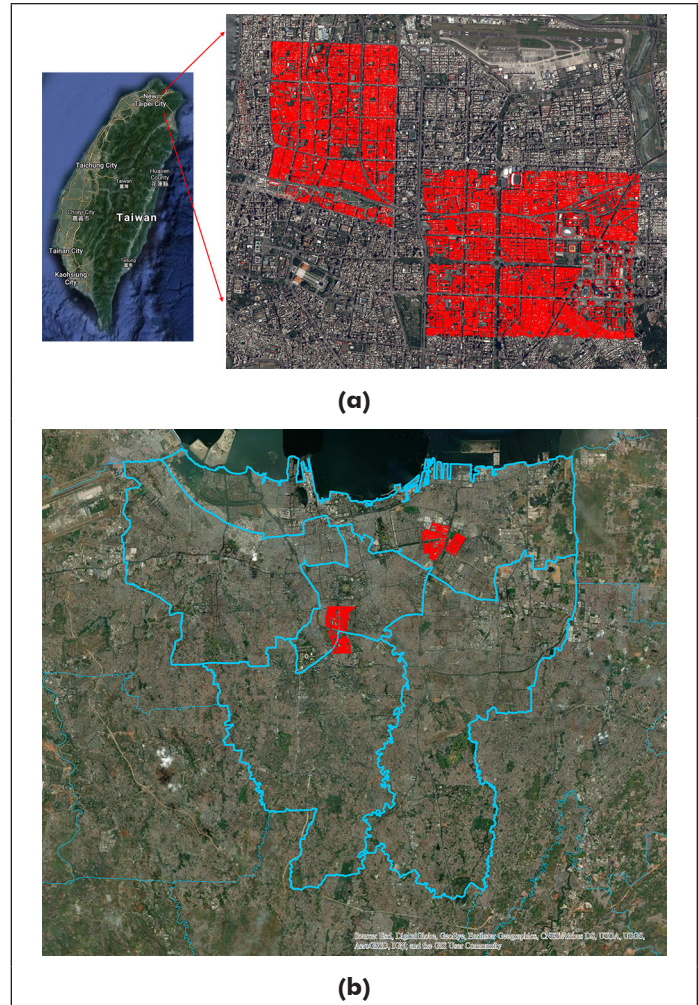


Figure 1. Study areas comprising (a) Taipei pilot area and (b) Jakarta city with its five regions. Test areas are indicated in red.

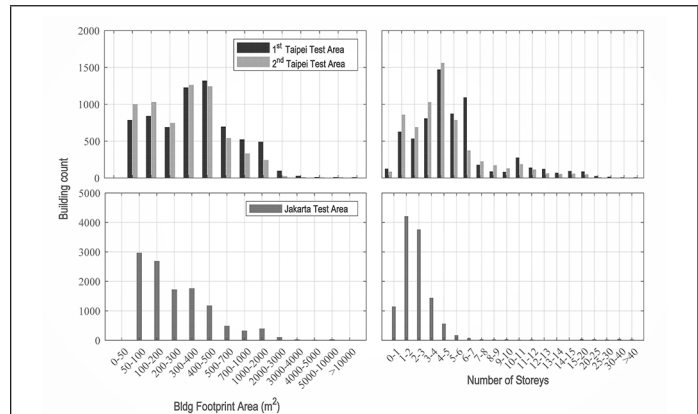


Figure 2. Distribution of building footprint (BFT) area and building height in ground reference data for test areas of Taipei (upper panels) and Jakarta (lower panels). An inter-story height of 3.45 m was used to covert height values to stories.

Regarding sources of satellite stereo images, images from WorldView series, *GeoEye-1*, *QuickBird*, *Pleiades 1A/1B* series, *KOMPSAT-3A/3A*, *CARTOSAT*, and *DMC3/Triple Sat* were evaluated for suitability. The *Pleiades 1A/1B* series were chosen as it allowed tight stereo angle specifications, providing ortho-rectified color data at 0.5 m resolution with high revisit interval of ~two days over Southeast

Asia. A tight stereo angle control was needed to capture tall buildings, while a high revisit rate allowed for cloud/mist free images even in wet, tropical regions, such as that for Jakarta. However, it should be noted that with the rapid advances in commercial satellite imaging, other satellite imagery that meet or exceed these requirements can equally be used.

Building Footprint and Height Extraction

Figure 3 shows a schematic of the BFT extraction methodology. A high degree of automation was achieved via use of RSP, *eCognition* and Geographical Information System (GIS) software, augmented with internally developed software. For DSM generation, the recently available RSP software shown to be particularly suited for use with large scale satellite stereo images (Qin 2016), and the more conventional SOCET GXP (GXP) are assessed with improved results using RSP obtained. In particular, DSM generation in RSP was performed by applying aerial triangulation, referring to ground control points and image matching.

The BFT shape extraction comprise automated segmentation with edge regularization along with a manual adjustment on a small percentage of extracted polygons (Figure 3). The segmentation and regularization procedures followed that of Kuo et al. (2018) and Su et al. (2015). Segmentation was applied only on preprocessed, built-up areas with roads and vegetation surfaces removed. Road surfaces were defined using road vectors from Open Street Map (OSM), with a road buffer width ranging from 1 m (small alleys) to 60 m (arterial road) applied as depending on the road type. Vegetation areas were classified using a Normalized Difference Vegetation Index (NDVI) (Huete et al. 2002), which is a normalized ratio of near infrared (IR) and red bands. Here a calibrated cut-off NDVI value of 0.25 was applied. The *eCognition* software was used for image segmentation on an Object Height Model (OHM), being the difference between DSM and DEM, for high-rise building, and on ortho-rectified images for low-rise buildings, following the segmentation algorithm of Baatz and Schäpe (2000). The first segmentation was exercised on an edge-preserving Kuwahara filtered (sharpened) OHM covering the built-up area following a

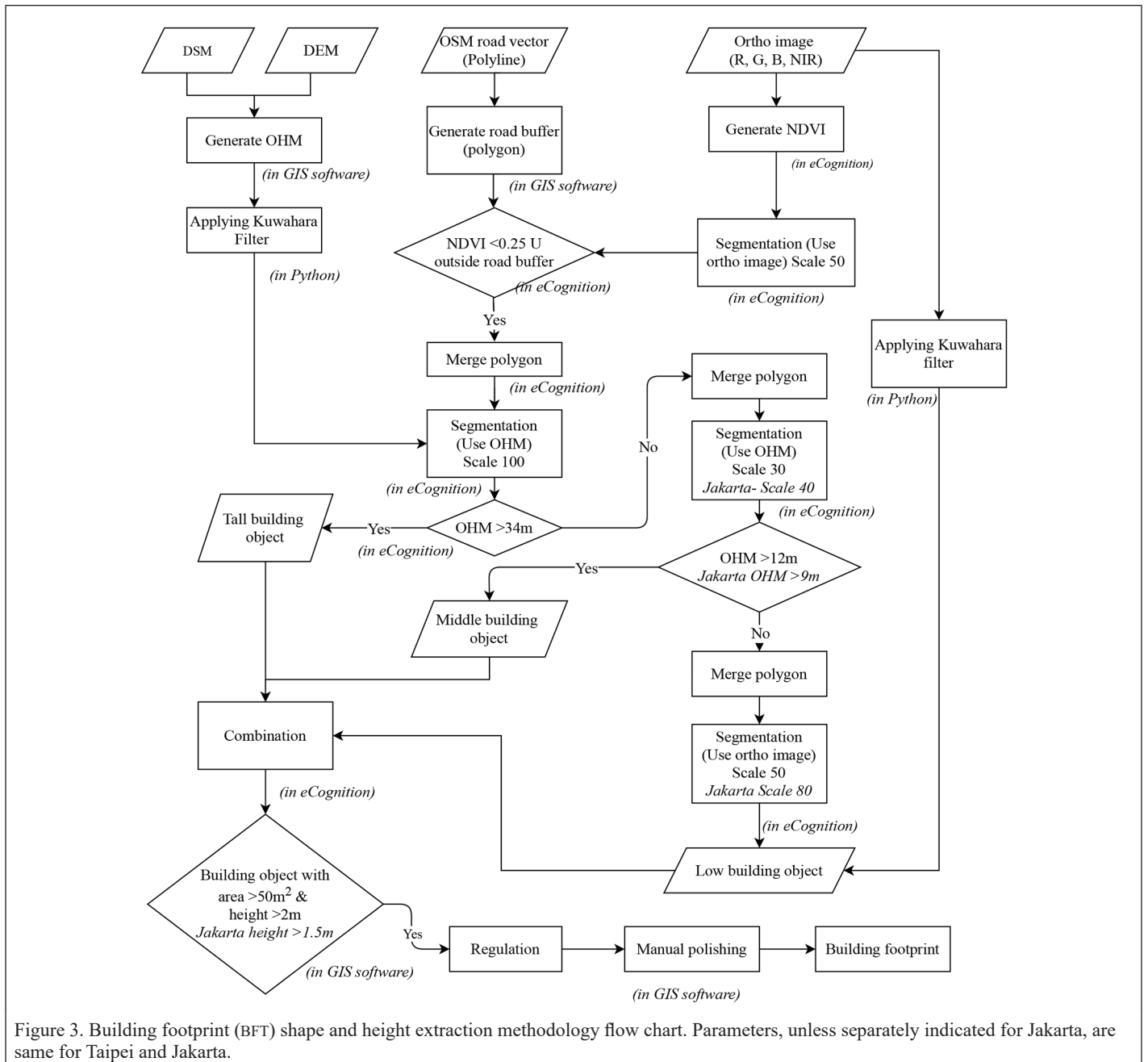


Figure 3. Building footprint (BFT) shape and height extraction methodology flow chart. Parameters, unless separately indicated for Jakarta, are same for Taipei and Jakarta.

building categorization based elevation values (see Figure 3). Regions with high elevations corresponded to larger building objects, which necessitated a larger scale parameter. For low elevation buildings, use of OHM consistently produced over-segmentation with many small objects identified. Rather segmentation on ortho-rectified color images produced satisfactory results for the low elevation buildings. Since the segmentation was based roof top elevations (high- and mid-elevation regions) and roof top features (low elevation region), the segmented objects were found to be sensitive to smaller roof top structures such as lift shafts, water tanks, or in the case of low residential buildings, small (often illegal) roof top additions. As these roof top features did not signify distinct buildings, adjacent polygons in mid- and low-elevation regions are merged if the height difference is less than 1.5 m. Polygons with BFT area $\leq 50 \text{ m}^2$ (nonbuildable land lots) or height $\leq 2 \text{ m}$ (i.e., nonbuilding objects of low height) were also removed.

The regularization step following Kuo et al. (2018) is to partially correct for jagged lines in the segmented polygon shapes, removing/merging small, extraneous extracted polygons, and straightening of polygon edges. In dense urban areas such as Taipei and Jakarta, many buildings are connected to each other and edges between such adjacent buildings would share the same geometry. These shared edges were simplified and regularized simultaneously to retain the shared edge. A small percentage of the polygons required manual adjustment on footprints by cross-comparison with Google maps and Google Streetview. Manual polishing is conducted on larger size buildings as defined by total floor area (TFA) being $\geq 8000 \text{ m}^2$ for Taipei and $\geq 2500 \text{ m}^2$ for Jakarta. This comprised less than 10% total number of buildings and indeed this 10% value was used as a guide in setting the TFA cutoff values for the city-specific larger buildings and thus, the manual effort required. After BFT shape extraction, building height was determined by averaging the OHM values within the extracted polygon shape with allowance of a boundary buffer and removal of outliers. In setting the TFA, an inter-story height of 3.45 m representing an average story height (residential 3.3 m and commercial 3.6 m) in Taipei and Jakarta is used for converting extracted building height to number of stories, which when multiplied by the BFT area gives the TFA.

The extraction methodology development involved a trial-and-error process as guided by a comparison of the extracted building polygons with the ground reference TVD data from Taipei first test area and using Taipei second test area as verification. The parameters of the extraction methodology are expected to have values for Jakarta different from Taipei's due to their different building characteristics (see Figure 2). These are tuned as guided by results from the Jakarta test areas. The notable differences are: $<9 \text{ m}$ building height is defined as low rise buildings in Jakarta while $<12 \text{ m}$ is used for Taipei. The segmentation scale for middle and low rise are, respectively, 40 and 80 for Jakarta, while they are 30 and 50 for Taipei. All processing unless otherwise indicated, are done within an ArcGIS environment. The most time intensive step is in the manual polishing performed on the small number of large, extracted building polygons. This required a modest 40 man-weeks (four summer interns were deployed) to cover whole Jakarta spanning 643 km^2 .

Performance Evaluation

The detected building polygon areas are first assessed for an overall building area detection performance via standard metrics of True Positive/Negative (TP/TN) and False Positive/Negative (FP/FN). Here TP/TN denote areas correctly classified as spanning buildings/non-building areas, FP denotes area incorrectly classified as building area, and FN as area incorrectly classified as nonbuilding area. From these, quality metrics of quality percentage (QP), detection rate (DR), and overall accuracy (OA) are computed. QP accounts for both boundary delineation accuracy and building detection rate, DR denotes the percentage building area correctly detected, and OA the percentage of building and non-building areas correctly detected.

$$QP = \frac{TP}{TP + FP + FN}; DR = \frac{TP}{TP + FN}; OA = \frac{TP + TN}{TP + TN + FP + FN} \quad (1)$$

However, beyond such metrics on overall building area being accurately detected, the individually extracted buildings (or polygons) do not necessarily have one-to-one match with the actual, with a common challenge of closely spaced buildings being extracted as one building in dense urban settings. This necessitated a more detailed object-level accuracy assessment, as achieved here by categorizing the extracted polygons into five cases below:

- Case 1 (extraneous): An extraneous polygon when the centroid of the extracted polygon does not fall within the boundary of any ground reference polygon.
- Case 2 (one-to-one): One-to-one (desired) match between an extracted polygon and a ground reference polygon. Here the centroids of extracted polygon and ground reference polygon fall within the boundaries of each other.
- Case 3 (one-to-many): The extracted polygon enclosed several ground reference polygons as defined by the centroids of the ground reference polygons falling within the boundary of the extracted polygon.
- Case 4 (many-to-one): Multiple polygons are extracted from one single ground reference polygon, and the boundary of the ground reference polygon encompasses the centroids of several extracted polygons.
- Case 5 (missed): Polygon missed in extraction.

Case 3 occurs when a cluster of tightly spaced ground reference buildings of similar height and inseparable from aerial views are grouped together in the extracted polygon (see Figure 4a). This often happens in dense urban settings with a prevalence of rows of tightly-spaced, inseparable buildings. Case 4 corresponds to buildings with complex roof top configurations or features resulting in multiple polygons being extracted within a single ground reference polygon (Figure 4b). As such, a count accuracy analysis across the five cases is first performed before an accuracy evaluation on the values of extracted BFT area and height. The analysis is performed separately for Taipei first test area (used for methodology development, i.e., a calibration) and tested independently over the second test area (i.e., a verification).

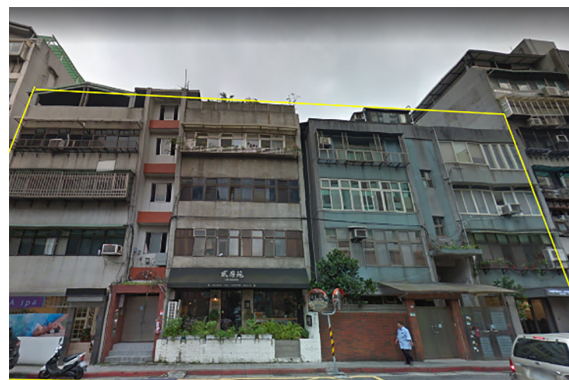
Results and Discussion

DSM generation using RSP and the more conventional GXP were first quantitatively compared for the Taipei test areas. Building rooftop elevations from TVD (subset of 125 buildings) are used to determine convergence angle requirements in the satellite stereo imagery needed for capturing tall buildings. The 125 TVD elevation values ranged up to 174 m, with a further value at 391 m corresponding to the super tall Taipei 101. Building rooftop elevation values calculated using RSP are more accurate than using GXP with regions of higher elevation having better delineation. Over 92% of the 125 buildings have elevation error $<3 \text{ m}$ at 14° convergence angle, this improving to 94% at 10° . The sole exception is Taipei 101, where RSP significantly underestimated and GXP even more so. The subsequent images used below for Jakarta are at 12° convergence angle. For OHM generation, a DEM was derived by sampling the RSP generated DSM ground points in free space such as parks and roads. A total of 432 ground points within and around the Taipei test areas are interpolated for DEM generation.

Figure 5 shows the extracted BFT polygons for the Taipei and Jakarta test areas. QP, DR, and OA values for Taipei first test area are 71.4%, 83.9%, and 87.5%, respectively, and 73.6%, 85.6%, and 86.8%, respectively, for the second test area. These values are within reported ranges for building detection applications from satellite imagery (Hermosilla et al. 2011; Ghandour and Jezzini 2018; Jin and Davis 2005; Lee et al. 2003), though higher ranges are reported by Khoshelham et al. (2010) who used multi-source (including lidar) data. The QP, DR, and OA values are 79.3%, 88.3%, and 91.4%, for the Jakarta test areas, slightly better than Taipei's.



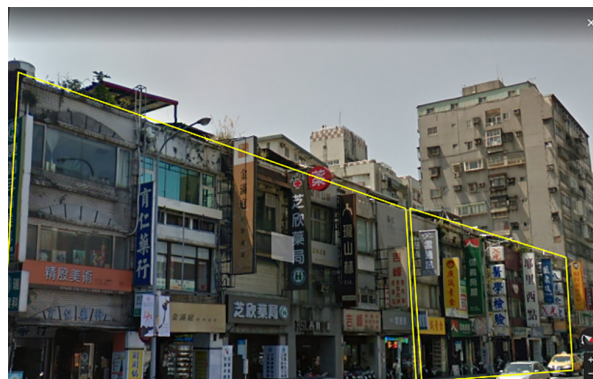
□ TVD □ Extracted polygons



(a)



□ TVD □ Extracted polygons



(b)

Figure 4. Buildings categorized as (a) Case 3: unseparated buildings due to small separation and small difference in roof height and (b) Case 4: over-segmented due to various rooftop structures. Examples shown are from Taipei test areas.



(a) Extracted BFT - Taipei 1st test area



(b) Extracted BFT - Taipei 2nd test area



(c) Extracted BFT - Jakarta test areas

Figure 5. Samples of extracted building footprint (BFT) from Taipei and Jakarta test areas.

Taipei Test Areas

The number of building polygons falling in each Case 1 to 5 are shown in Table 1 for Taipei's two test areas individually and combined. Focusing on the first test (calibration) area, 46.9% of the extracted polygons have a one-to-one (Case 2, ideal) extraction, while Cases 2 and 3 combined totals 67.0%. For estimating total building value exposed to hazards, Cases 3 and 4 as representing dense building clusters would also be considered as correct extraction. This is because Case 3 has one extracted building (polygon) encompassing several tightly-spaced, i.e., essentially inseparable buildings that would be very similar in height and in structural characteristics, and therefore in building exposure and vulnerability characteristics. This also applies for Case 4 where several extracted building polygons with very similar characteristics collectively represent one actual building. With this, the combined polygons over Cases 2, 3, and 4 comprise 95.07% of the extracted. Only a small percentage at 4.93% are in Case 1 (extraneous) polygons. It is noted these percentage counts are based on the total extracted polygon count (i.e., Sum Cases 1 to 4). The number of missed polygons (Case 5) is 713, i.e. 13.5% relative to the total number of extracted polygons. Similar extraction performance is seen for Taipei second test (verification) area. The extracted have 50.7% one-on-one (Case 2), and 95.3% in combined Cases 2, 3, and 4, with only a small 4.71% Case 1 (extraneous polygon). The number of missed polygons (Case 5) is 440, i.e., 8.5% relative to the total number extracted.

The extraction performance, particularly Case 2, is improved for the larger TFA building polygons (Table 1). For building TFA >4000 m², Case 2 extraction is slightly improved at 51.8% from 48.8% for the combined Taipei test areas and improving significantly to 71.9% for TFA >8000 m². Thus, progressively more of the larger buildings, and thus building values exposed to hazards, are extracted on one-to-one basis. The percentage in extracted Cases 3 and 4 (i.e., building clusters) is essentially unchanged for TFA >4000 m², but notably reduced for TFA >8000 m² at 27.4%. Greater than 99% accuracy over combined Cases 2 to 4 is achieved for the larger buildings with TFA >4000 m² and >8000 m² (Table 1); this also holds for the individual test areas (not shown).

The percentage distribution of building polygon counts across Cases 1–5 and cumulative for Taipei's combined test areas are plotted in TFA bins (Figure 6). It is evident that Case 2 (one-to-one) extraction (red bars) becomes dominant at larger building TFA bins. In contrast,

Case 1's 506 extraneous polygons (Table 1) and Case 5's 1153 missed polygons were mostly confined to buildings with small TFA of <1000 m². This again indicates that the larger buildings are better extracted. Successfully capturing such large buildings is key towards capturing the city's entire built-up TFA, and thus a city's inventory of building values and exposure. Thus Figure 6 shows that the larger TFA >8000 m² buildings contributing 43% of the test areas' cumulative TFA.

Detailed error analysis on extracted BFT area and height values are next discussed considering Cases 2, 3, and 4 individually, and covering Taipei first (calibration) and second (verification) test area separately. Table 2 summarizes the BFT area error, dA, for all buildings and building with large TFA >4000 m² and >8000 m². The results show that 67–74% of all buildings in Cases 2 and 3 had error abs(dA) <30% across the two test areas. In this error calculation, Case 3 used the total BFT areas of the encompassed ground truth (TVD) buildings as these are corresponded to tightly-spaced, inseparable buildings. As expected, there is a significant improvement for the larger TFA buildings where 71–89% in Cases 2 and 3 has abs(dA) <30% for building with TFA >4000 m², and >92% for TFA >8000 m². By comparison, the errors for

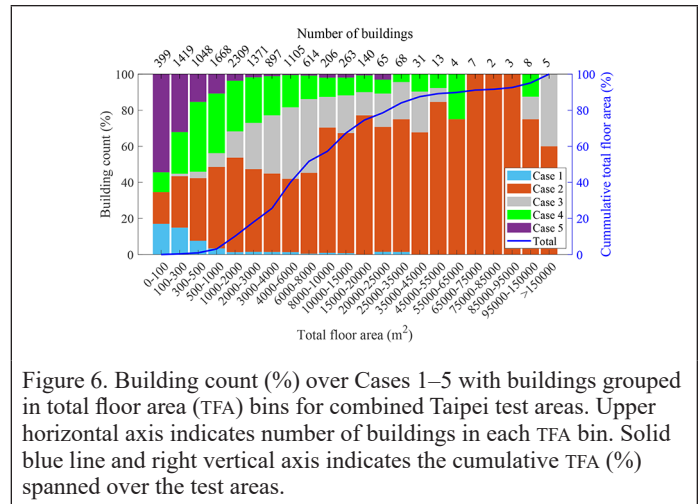


Figure 6. Building count (%) over Cases 1–5 with buildings grouped in total floor area (TFA) bins for combined Taipei test areas. Upper horizontal axis indicates number of buildings in each TFA bin. Solid blue line and right vertical axis indicates the cumulative TFA (%) spanned over the test areas.

Table 1. Count Analysis across Cases 1 to 5 building polygons for Taipei and Jakarta test areas. Percentage numbers in parentheses are based on number of extracted polygons (sum Cases 1 to 4).

| Case | Taipei | | | | | Jakarta Test Area | | |
|--------------------------------------|----------------------------------|------------------------------------|---------------------|--------------------------|--------------------------|-------------------|--------------------------|--------------------------|
| | First Test Area (Calibration) | Second Test Area (Verification) | Combined Test Areas | | | All | TFA >4000 m ² | TFA >8000 m ² |
| | | | All | TFA >4000 m ² | TFA >8000 m ² | | | |
| 1 (extraneous), n (%) | 261 (4.93) | 245 (4.71) | 506 (4.82) | 24 (0.96) | 6 (0.75) | 642 (6.49) | 3 (0.53) | 1 (0.28) |
| 2 (one-to-one), n (%) | 2485 (46.9) | 2635 (50.7) | 5120 (48.8) | 1301 (51.8) | 577 (71.9) | 4851 (49.0) | 481 (85.1) | 299 (84.2) |
| 3 (one to many), n (%) | 1065 (20.1) | 928 (17.9) | 1993 (19.0) | 834 (33.2) | 145 (18.1) | 1793 (18.1) | 61 (10.8) | 46 (13.0) |
| 4 (many to one), n (%) | 1483 (28.0) | 1390 (26.7) | 2873 (27.4) | 352 (14.0) | 75 (9.3) | 2606 (26.3) | 20 (3.5) | 9 (2.5) |
| 5 (missed) | [713] | [440] | [1153] | [23] | [12] | [1043] | [8] | [1] |
| Total Extracted (Sum Cases 1 to 4) | 5294 | 5198 | 10,492 | 2511 | 803 | 9892 | 565 | 355 |
| Sum Cases 2 to 4/Total Extracted (%) | 95 | 95.3 | 95.2 | 99.0 | 99.3 | 93.4 | 99.5 | 99.7 |

TFA = total floor area.

Table 2. Count and percentage of buildings in Taipei test areas with building footprint error abs(dA) < 20% and < 30%.

| Case | | Taipei First Test Area | | | | | | Taipei Second Test Area | | | | | |
|--------|---------------|------------------------|----|--------------------------|----|--------------------------|----|-------------------------|----|--------------------------|----|--------------------------|-----|
| | | All buildings | | TFA >4000 m ² | | TFA >8000 m ² | | All buildings | | TFA >4000 m ² | | TFA >8000 m ² | |
| | | Count | % | Count | % | Count | % | Count | % | Count | % | Count | % |
| Case 2 | abs(dA) < 20% | 1345/2485 | 54 | 600/783 | 77 | 330/376 | 88 | 1493/2635 | 57 | 376/518 | 73 | 160/201 | 80 |
| | abs(dA) < 30% | 1672/2485 | 67 | 678/783 | 87 | 356/376 | 95 | 1864/2635 | 71 | 459/518 | 89 | 188/201 | 94 |
| Case 3 | abs(dA) < 20% | 580/1065 | 54 | 274/505 | 54 | 92/118 | 78 | 514/928 | 55 | 185/329 | 56 | 14/27 | 89 |
| | abs(dA) < 30% | 759/1065 | 71 | 359/505 | 71 | 108/118 | 92 | 685/928 | 74 | 244/329 | 74 | 27/27 | 100 |
| Case 4 | abs(dA) < 20% | 121/1483 | 8 | 47/230 | 20 | 8/40 | 20 | 114/1390 | 8 | 23/122 | 19 | 6/35 | 17 |
| | abs(dA) < 30% | 204/1483 | 14 | 69/230 | 30 | 11/40 | 28 | 176/1390 | 13 | 36/122 | 30 | 7/35 | 20 |

TFA = total floor area.

Case 4 buildings are much larger, as expected, since the one extracted polygon encompassed several TVD polygons, but only one TVD polygon was matched with the extracted for the dA error calculation.

Table 3 shows the errors dH in the extracted building heights. For Taipei first (calibration) test area, 91% and 94% of all buildings in Case 2 and 3, respectively had $\text{abs}(dH) < 3$ m and with the accuracy being essentially unchanged for the larger TFA buildings, whilst 81% of all buildings in Case 4 had $\text{abs}(dH) < 3$ m. The height accuracy for the second (verification) test area was less by comparison, which was attributed to the TVD height values being less accurate due to this area being in an older part of Taipei with older TVD.

The Mean Absolute Errors (MAE) for BFT area, height, and TFA are listed in Table 4 for the combined Taipei test areas. Results at four TFA ranges are shown, comprising all TFA values, $TFA \leq 4000$ m², TFA between 4000 m²–8000 m², and TFA >8000 m². While the MAE values on both BFT area and TFA over all buildings (all TFA values) are high at 37%–40%, the values are much reduced for buildings with TFA between 4000–8000 m² and TFA >8,000 m², with the MAE in TFA being at 29% and 17%, respectively.

The scalability of the building extraction algorithm is next demonstrated by applying the extraction framework to the full Taipei pilot area of 27.9 km² (see Figure 7a). In total, 20,597 building polygons are extracted, of which 2355 are with large BFT area (>1000 m²) and 1957 have height >10 floors. Also 47% (i.e., almost half) of the entire TFA over the pilot area is contributed by the larger buildings (TFA >8000 m²); these buildings comprise only 9% of total building count. Furthermore, these buildings are expected to have small MAE as their extracted BFT area, height, and TFA (Table 4).

Jakarta City

The full scalability of the building extraction is demonstrated for the megacity of Jakarta covering an area of 643 km². The extraction algorithm parameters are first tuned using the Jakarta test areas' ground reference to account for building characteristics being different from Taipei's. The earlier Table 1 also shows the number of extracted building polygons from Jakarta test areas as falling into Cases 1 to 5. Compared to the Taipei test areas, the algorithm had comparable performance in Case 2 (one-to-one) extraction, and with a better improvement for the larger TFA buildings at 84%–85% extraction, with the percentages for Cases 3 and 4 correspondingly reduced. Case 1 extraneous and Case 5 missed polygons remain small as with Taipei's test

areas. Figure 8 plots the percentage distribution of building polygons counts across Cases 1–5 and cumulative for Jakarta's combined test areas against TFA bins (i.e., as shown earlier in Figure 6 for Taipei test areas). As with the Taipei test area results, Case 2 (one-to-one) extraction becomes dominant at large TFA bins, while Case 1 (extraneous) polygons and Case 5 missed polygons are mostly confined to small TFA bins. Similarly, the larger building contributed disproportionately to the cumulative TFA, e.g., building with TFA >4000 m² contributed 70.5% of Jakarta's test areas cumulative TFA.

In terms of dA errors on BFT area, 52.4% of all buildings are extracted with $\text{abs}(dA) < 30\%$, and further improved for larger TFA (>4000 m²) buildings at 92.9%. The error in building height dH has 75.7% of extracted buildings having $\text{abs}(dH) < 3$ m, and 75.4% (i.e., essentially unchanged) for the larger TFA (>4000 m²) buildings. The MAE values (Table 4) are comparable to that achieved for Taipei test areas, and better for the larger TFA buildings.

The algorithm extracted over 1.247 million buildings for the megacity of Jakarta (Figure 7b). Extracted BFT area, height, and TFA statistics are shown in Figure 9. Jakarta's buildings largely are low rise with 59% (32%) of the buildings are at one (two) story (Figure 9a), and only 1744 buildings having >10 stories. 78% of the buildings have BFT areas of 50–300 m², while only 13,302 buildings have BFT >1000 m² area (Figure 9b). Small TFA <4000 m² buildings contributes to 76% of Jakarta's entire TFA (Figure 9c), this representing 99% of the total number of buildings, whilst large buildings of TFA >8000 m² contributes 18% of Jakarta's entire TFA, i.e., a smaller percentage when compared to the Jakarta (also Taipei) test areas. This is because these test areas, being in their respective downtown core, are more populated with high-rise and large footprint buildings.

Conclusion

The work demonstrates a highly efficient and automated BFT and height extraction methodology using high-resolution satellite stereo images and off-the-shelf software, with an application to the megacity of Jakarta. The methodology is developed using small Taipei test areas where accurate ground reference TVD is available. Differences in building characteristics between the two cities are accounted for via tuning of algorithm parameters using small Jakarta test areas.

The results on extracted buildings are analyzed over the test areas, both on the extraction count over buildings, which can be closely

Table 3. Count and percentage of buildings in Taipei test areas with height error $\text{abs}(dH) < 2$ m and < 3 m.

| Case | | Taipei First Test Area | | | | | | Taipei Second Test Area | | | | | |
|--------|------------------------|------------------------|----|--------------------------|----|--------------------------|----|-------------------------|----|--------------------------|----|--------------------------|----|
| | | All buildings | | TFA >4000 m ² | | TFA >8000 m ² | | All buildings | | TFA >4000 m ² | | TFA >8000 m ² | |
| | | Count | % | Count | % | Count | % | Count | % | Count | % | Count | % |
| Case 2 | $\text{abs}(dH) < 2$ m | 2113/2485 | 85 | 675/783 | 86 | 316/376 | 84 | 1703/2635 | 65 | 312/518 | 60 | 101/201 | 50 |
| | $\text{abs}(dH) < 3$ m | 2263/2485 | 91 | 699/783 | 89 | 331/376 | 88 | 2116/2635 | 80 | 371/518 | 72 | 126/201 | 63 |
| Case 3 | $\text{abs}(dH) < 2$ m | 959/1065 | 90 | 457/505 | 90 | 99/118 | 84 | 729/928 | 79 | 269/329 | 82 | 23/27 | 85 |
| | $\text{abs}(dH) < 3$ m | 1001/1065 | 94 | 473/505 | 94 | 104/118 | 88 | 832/928 | 90 | 299/329 | 91 | 24/27 | 89 |
| Case 4 | $\text{abs}(dH) < 2$ m | 1045/1483 | 70 | 187/230 | 81 | 26/40 | 65 | 817/1390 | 59 | 62/122 | 51 | 14/35 | 40 |
| | $\text{abs}(dH) < 3$ m | 1201/1483 | 81 | 199/230 | 87 | 28/40 | 70 | 996/1390 | 72 | 76/122 | 62 | 18/35 | 51 |

TFA = total floor area.

Table 4. Mean Absolute Errors (MAE) (%) in building footprint (BFA), height, and total floor area (TFA) for buildings in the combined test areas of Taipei.

| Parameter | Taipei | | | | Jakarta | | | |
|------------|-------------------|--------------------------------|-------------------------------|--------------------------|-------------------|--------------------------------|-------------------------------|--------------------------|
| | All TFA buildings | TFA ≤ 4000 m ² | TFA: 4000–8000 m ² | TFA >8000 m ² | All TFA buildings | TFA ≤ 4000 m ² | TFA: 4000–8000 m ² | TFA >8000 m ² |
| BFT MAE | 37 | 42 | 27 | 16 | 37 | 39 | 9 | 8 |
| Height MAE | 12 | 14 | 8 | 7 | 28 | 29 | 14 | 8 |
| TFA MAE | 40 | 45 | 29 | 17 | 48 | 49 | 20 | 15 |

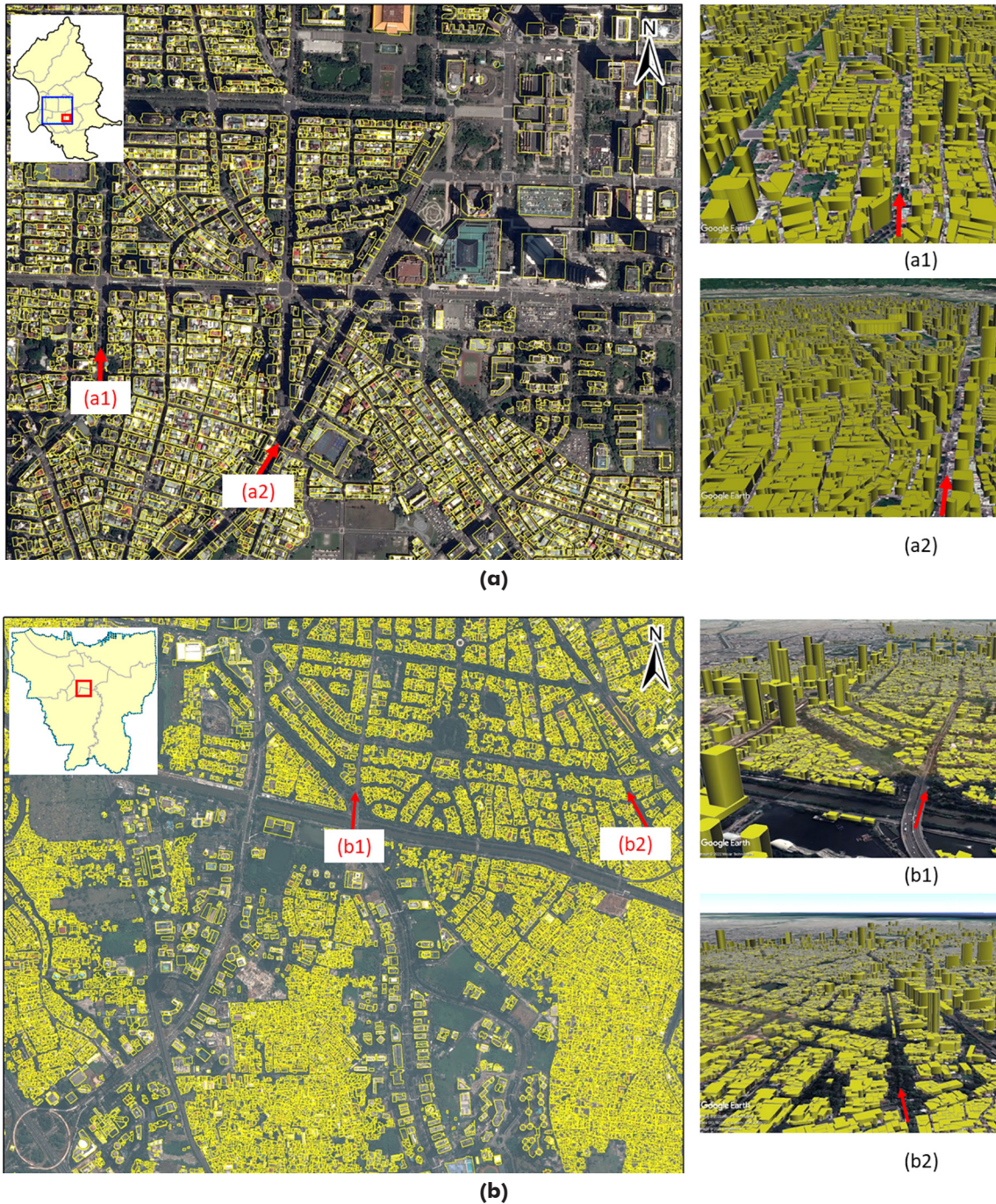


Figure 7. Building polygons extracted from (a) Taipei 27.9 km² pilot area and (b) Jakarta over 643 km². Solid blue lines in upper left inset indicate the full areal extent covered, and solid red lines show the areal extent of an expanded two-dimensional view with further detailed three-dimensional views shown in the left panels at locations indicated by the red arrows.

spaced in dense urban areas, and on errors in the extracted BFT area, height, and TFA. It is shown that buildings captured in Taipei test areas are at one-to-one (Case 2) extraction for 48.8% of the captured buildings, improving to 71.9% for larger buildings with TFA >8000 m², and further reaches 99% accuracy when closely-spaced, inseparable building clusters of similar height and structural characteristics are included, as appropriate for building exposure development. Extraneous and missed building were small in number, and notably are largely confined to small TFA buildings. The MAE in BFT area, while being at 37% over all captured buildings, reduced significantly to 27% for larger TFA buildings (TFA between 4000–8000 m²), and to 16% for buildings with

TFA >8000 m². Similar extraction performance and accuracies hold for the Jakarta test areas. It is also shown that the larger TFA buildings, while small in count number, contributes disproportionately to the cumulative TFA for both Taipei and Jakarta test areas, e.g., Jakarta's test areas located in the downtown core have buildings with TFA >4000 m² contributing to 70.5% of the cumulative TFA, whilst over the entire Jakarta of 643 km², such buildings with >4000 m² TFA contributes 24% of the cumulative TFA.

The analyses indicate that the extraction methodology is effective, even for megacities, accurately capturing building inventory covering areas and heights via readily available satellite imagery. This provides

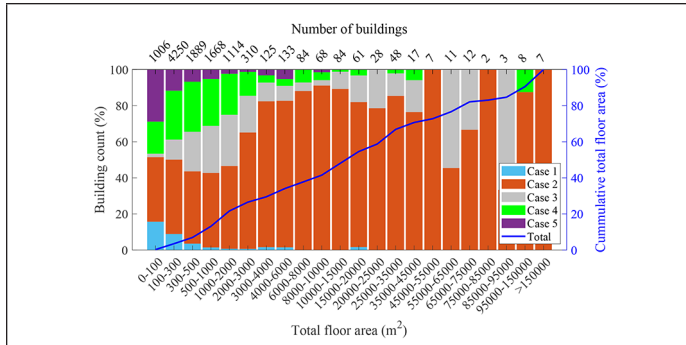


Figure 8. Building count (%) over Cases 1–5 with buildings grouped in total floor area (TFA) bins for combined Jakarta test areas. Upper horizontal axis indicates number of buildings in each TFA bin. Solid blue line and right vertical axis indicates the cumulative TFA (%) spanned over the test areas.

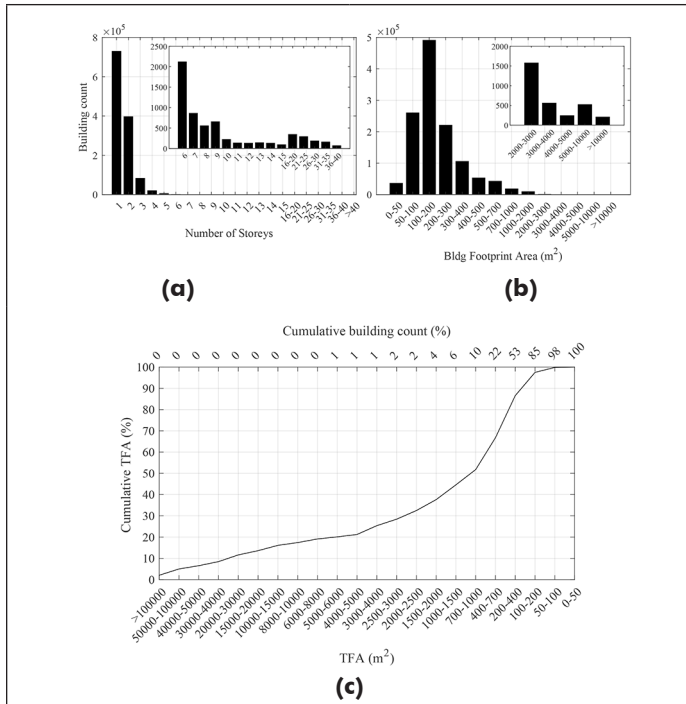


Figure 9. Statistics on buildings in Jakarta. Note in (c) total floor area (TFA) bins are plotted in decreasing bin size and the upper horizontal axis indicate cumulative building count (%).

a cost-effective, readily deployable option for quantifying city-wide building inventory needed in city planning, and for risk analysis under hazards. It would therefore find use in national and regional government units involved in disaster planning and management. Lastly, the extraction methodology can readily take advantage of increasingly more accurate satellite imagery or aerial/UAV images as they become available.

References

Awrangzeb, M., M. Ravanbakhsh and C. S. Fraser. 2010. Automatic detection of residential buildings using LIDAR data and multispectral imagery. *ISPRS Journal of Photogrammetry and Remote Sensing* 65(5):457–467.

Baatz, M. and A. Schäpe. 2000. Multiresolution segmentation: An optimization approach for high quality multi-scale image segmentation. Pages 12–23 in *Proceedings Angewandte Geographische Informationsverarbeitung XII, Beiträge zum AGIT-Symposium Salzburg 2000*. Edited by J. Strobl. Karlsruhe, Germany: Herbert Wichmann Verlag.

Belgiu, M. and L. Drăguț. 2014. Comparing supervised and unsupervised multiresolution segmentation approaches for extracting buildings from very high resolution imagery. *ISPRS Journal of Photogrammetry and Remote Sensing* 96:67–75.

Bittner, K., F. Adam, S. Cui, M. Körner and P. Reinartz. 2018. Building footprint extraction from VHR remote sensing images combined with normalized DSMs using fused fully convolutional networks. *IEEE Journal of Selected Topics in Applied Earth Observations and Remote Sensing* 11(8):2615–2629.

Chen, R., X. Li and J. Li. 2018. Object-based features for house detection from RGB high-resolution images. *Remote Sensing* 10(3):451.

De Angeli, S., F. Dell’Acqua and E. Trasforini. 2016. Application of an earth-observation-based building exposure mapping tool for flood damage assessment. In *Proceedings 3rd European Conference on Flood Risk Management (FLOODrisk 2016)*. Edited by M. Lang, F. Klijn and P. Samuels. *EDP Science*. <https://doi.org/10.1051/e3sconf/20160705001>.

Figueiredo, R. and M. Martina. 2016. Using open building data in the development of exposure data sets for catastrophe risk modelling. *Natural Hazards and Earth System Sciences* 16(2):417–429. <https://doi.org/10.5194/nhess-16-417-2016>.

Garcia-Garcia, A., S. Orts, S. Oprea, V. Villena-Martinez and J. G. Rodriguez. 2017. A review on deep learning techniques applied to semantic segmentation. arXiv:1704.06857v1.

Gavankar, N. L. and S. K. Ghosh. 2018. Automatic building footprint extraction from high-resolution satellite image using mathematical morphology. *European Journal of Remote Sensing* 51(1):182–193. <https://doi.org/10.1080/22797254.2017.1416676>.

Gui, S. and R. Qin. 2021. Automated LoD-2 model reconstruction from very-high-resolution satellite-derived digital surface model and orthophoto. *ISPRS Journal of Photogrammetry and Remote Sensing* 181:1–19.

Ghandour, A. J. and A. A. Jezzini. 2018. Autonomous building detection using edge properties and image color invariants. *Buildings* 8(5):65.

Grossi, P., H. Kunreuther and D. Windeler. 2005. An introduction to catastrophe models and insurance. In *Catastrophe Modeling: A New Approach to Managing Risk*, edited by P. Grossi and H. Kunreuther, 23–42. Boston, Massachusetts: Springer.

Gunasekera, R., O. Ishizawa, C. Aubrecht, B. Blankespoor, S. Murray, A. Pomonis and J. Daniell. 2015. Developing an adaptive global exposure model to support the generation of country disaster risk profiles. *Earth-Science Reviews* 150:594–608. <https://doi.org/10.1016/j.earscirev.2015.08.012>.

Haitcoat, T. L., W. Song and J. D. Hipple. 2001. Building footprint extraction and 3-D reconstruction from LIDAR data. In *Proceedings IEEE/ISPRS Joint Workshop on Remote Sensing and Data Fusion over Urban Areas (Cat. No.01EX482)*, held in Rome, Italy, 8–9 November 2001. <https://doi.org/10.1109/DFUA.2001.985730>.

Hermosilla, T., L. A. Ruiz, J. A. Recio and J. Estornell. 2011. Evaluation of automatic building detection approaches combining high resolution images and lidar data. *Remote Sensing* 3(6):1188–1210.

Huang, X. and L. Zhang. 2012. Morphological building/shadow index for building extraction from high-resolution imagery over urban areas. *IEEE Journal of Selected Topics in Applied Earth Observations and Remote Sensing* 5(1):161–172. <https://doi.org/10.1109/JSTARS.2011.2168195>.

Huete, A., K. Didan, T. Miura, E. P. Rodriguez, X. Gao and L. G. Ferreira. 2002. Overview of the radiometric and biophysical performance of the MODIS vegetation indices. *Remote Sensing of Environment* 83(1):195–213. [https://doi.org/10.1016/S0034-4257\(02\)00096-2](https://doi.org/10.1016/S0034-4257(02)00096-2).

Im, J., L. J. Quackenbush, M. Li and F. Fang. 2014. Optimum scale in object-based image analysis. In *Scale Issues in Remote Sensing*, edited by Q. Weng. Hoboken, New Jersey: Wiley. <https://doi.org/10.1002/9781118801628.ch10>.

Jin, X. and C. H. Davis. 2005. Automated building extraction from high-resolution satellite imagery in urban areas using structural, contextual, and spectral information. *EURASIP Journal on Advances in Signal Processing* (14):745309. <https://doi.org/10.1155/ASP.2005.2196>.

Khoshelham, K., C. Nardinocchi, E. Frontoni, A. Mancini and P. Zingaretti. 2010. Performance evaluation of automated approaches to building detection in multi-source aerial data. *ISPRS Journal of Photogrammetry and Remote Sensing* 65(1):123–133. <https://doi.org/10.1016/j.isprs.2009.09.005>.

- Kuo, H.-Y., J.-Y. Rau and EY.-M. Lo. 2018. Building footprint regulation assisted by road vector derived from open street map. *Proceedings International Symposium on Remote Sensing*, held in Pyeongchang, Korea, 9–11 May 2018.
- Lee, D. S., J. Shan and J. S. Bethel. 2003. Class-guided building extraction from Ikonos imagery. *Photogrammetric Engineering & Remote Sensing* 69(2):143–150. <https://doi.org/10.14358/PERS.69.2.143>.
- Li, W., C. He, J. Fang, J. Zheng, H. Fu and L. Yu. 2019. Semantic segmentation-based building footprint extraction using very high-resolution satellite images and multi-source GIS data. *Remote Sensing* 11(4):403.
- Lu, T., D. Ming, X. Lin, Z. Hong, X. Bai and J. Fang. 2018. Detecting building edges from high spatial resolution remote sensing imagery using richer convolution features network. *Remote Sensing* 10(9):1496.
- Maltezos, E., A. Doulamis, N. Doulamis and C. Ioannidis. 2019. Building extraction from LiDAR data applying deep convolutional neural networks. *IEEE Geoscience and Remote Sensing Letters* 16(1):155–159.
- Minaee, S., Y. Y. Boykov, F. Porikli, A. J. Plaza, N. Kehtarnavaz and D. Terzopoulos. 2021. Image segmentation using deep learning: A survey. *IEEE Transactions on Pattern Analysis and Machine Intelligence*. <https://doi.org/10.1109/TPAMI.2021.3059968>.
- NatCatSERVICE–Munich Re. 2019. Münchener Rückversicherungs-Gesellschaft (Munich Reinsurance Company). <<https://natcatservice.munichre.com>> Accessed 26 March 2021.
- Ok, A. O. 2013. Automated detection of buildings from single VHR multispectral images using shadow information and graph cuts. *ISPRS Journal of Photogrammetry and Remote Sensing* 86:21–40. <https://doi.org/10.1016/j.isprsjprs.2013.09.004>.
- Qin, R. 2016. RPC stereo processor (RSP)—A software package for digital surface model and orthophoto generation from satellite stereo imagery. Pages 77–82 in *Proceedings ISPRS Annals of the Photogrammetry, Remote Sensing and Spatial Information Sciences*, held in Prague, Czech Republic, 12–19 July 2016. Copernicus Publications. <https://doi.org/10.5194/isprs-annals-III-1-77-2016>.
- Sahar, L., S. Muthukumar and S. P. French. 2010. Using aerial imagery and GIS in automated building footprint extraction and shape recognition for earthquake risk assessment of urban inventories. *IEEE Transactions on Geoscience and Remote Sensing* 48(9):3511–3520. <https://doi.org/10.1109/TGRS.2010.2047260>.
- Silva, V., H. Crowley, H. Varum and R. Pinho. 2015. Seismic risk assessment for mainland Portugal. *Bulletin of Earthquake Engineering* 13:429–457. <https://doi.org/10.1007/s10518-014-9630-0>.
- Su, G., W. Qi, S. Zhang, T. Sim, X. Liu, R. Sun, L. Sun and Y. Jin. 2015. An integrated method combining remote sensing data and local knowledge for the large-scale estimation of seismic loss risks to buildings in the context of rapid socioeconomic growth: A case study in Tangshan, China. *Remote Sensing* 7(3):2543.
- Sun, Y., X. Zhang, X. Zhao and Q. Xin. 2018. Extracting building boundaries from high resolution optical images and LiDAR data by integrating the convolutional neural network and the active contour model. *Remote Sensing* 10(9):1459.
- Wei, S., S. Ji and M. Lu. 2020. Toward automatic building footprint delineation from aerial images using CNN and regularization. *IEEE Transactions on Geoscience and Remote Sensing* 58(3):2178–2189.
- Xu, Y., L. Wu, Z. Xie and Z. Chen. 2018. Building extraction in very high resolution remote sensing imagery using deep learning and guided filters. *Remote Sensing* 10(1):144.
- Yu, D., S. Ji, J. Liu and S. Wei. 2021. Automatic 3D building reconstruction from multi-view aerial images with deep learning. *ISPRS Journal of Photogrammetry and Remote Sensing* 171:155–170.
- Yuan, J. 2018. Learning building extraction in aerial scenes with convolutional networks. *IEEE Transactions on Pattern Analysis and Machine Intelligence* 40(11):2793–2798. <https://doi.org/10.1109/TPAMI.2017.2750680>.
- Zhang, L., Z. Shao, J. Liu and Q. Cheng. 2019. Deep learning based retrieval of forest aboveground biomass from combined LiDAR and Landsat 8 data. *Remote Sensing* 11(12). <https://doi.org/10.3390/rs11121459>.
- Zhang, L. and L. Zhang. 2018. Deep learning-based classification and reconstruction of residential scenes from large-scale point clouds. *IEEE Transactions on Geoscience and Remote Sensing* 56(4):1887–1897.

IN-PRESS ARTICLES

- Sunil Kumar Pundir, Rahul Dev Garg. Development of technique for Vehicle specific off-road trafficability assessment using soil cone index, water index & geospatial data.
- Weidong Li, Fanqian Meng, Yongbo Yu. The use of indices and modified U-Net network in improving the classification of planting structures.
- Weiwei Liu. Managing earth hazards using deep reinforcement learning algorithm for industrial IoT network.
- Itiya Anece, Prasad S. Thenkabail. New generation hyperspectral sensors DESIS and PRISMA provide improved agricultural crop classifications.
- Yanzhe Shi, Yumin Tan, Yunxin Li, Bo Xu. Automatic registration method of multi-source point clouds based on building facades matching in urban scenes.
- Zhang Yan, Wang Xiangyu, Zhang Zhongwei, Sun Yemei, and Liu Shudong. Foreground-Aware Refinement Network for Building Extraction from Remote Sensing Images.
- Yumin Tan, Yanzhe Shi, Yunxin Li, and Bo Xu. Automatic registration method of multi-source point clouds based on building facades matching in urban scenes.
- Yan Lv, Hongwei Guo, Shuanggen Jin, Lu Wang, Haiyi Bian, and Haijian Liu. Permanganate index variations and factors in Hongze Lake from Landsat-8 images based on machine learning.
- Songjing Guo, Xueling Wu, Ruiqing Niu, and Wenfu Wu. Exploring spatiotemporal variations and driving factors of urban comprehensive carrying capacity in the Yangtze River Delta urban agglomeration.

A Semi-Supervised Learning Method for Hyperspectral-Image Open Set Classification

Zhaolin Duan, Hao Chen, Xiaohua Li, Jiliu Zhou, and Yuan Wang

Abstract

We present a conceptually simple and flexible method for hyperspectral-image open set classification. Unlike previous methods, where the abundant unlabeled data inherent in the data set are ignored completely and unknown classes are inferred using score post-calibration, our approach makes the unlabeled data join in and help to train a simple and practical model for open set classification. The model is able to provide an explicit decision score for both unknown classes and each known class. The main idea of the proposed method is augmenting the original training set of K known classes using the pseudo-labeled unknown-category samples that are detected elaborately from the unlabeled data using modified OpenMax and semi-supervised iterative learning. Then a $(K + 1)$ -class deep convolutional neural network model is trained based on the augmented training set with $(K + 1)$ class samples. The model can not only classify instances of each known class but also refuse instances of unknown class explicitly. We validated the proposed method on four well-known hyperspectral-image data sets, obtaining superior performance over previous methods.

Introduction

A hyperspectral image (HSI) consists of hundreds of narrow contiguous-wavelength bands carrying a wealth of spectral information. Taking advantage of the rich spectral information, hyperspectral data are extremely useful in a wide range of applications in remote sensing, such as urban monitoring (Fauvel *et al.* 2008), agriculture (Lanthier *et al.* 2008), change or target detection (Mercier and Girard-Arduin 2006; Bovolo 2009). Hyperspectral-image classification, which assigns each pixel to one certain category based on its characteristics, is the most vibrant field of research in the hyperspectral community and has drawn broad attention in the remote sensing field (S. Li *et al.* 2019).

Hyperspectral-image classification (HSIC) methods can be divided into those based on spectral features and those based on spectral-spatial features, according to the input information used. In early research attempts, the spectral vector of the pixel was intuitively used for classification to take advantage of abundant spectral bands (Jia and Richards 1994; Murat Dundar and Landgrebe 2002; Bazi and Melgani 2006; J. Li *et al.* 2010). With the development of imaging technology, hyperspectral sensors can provide higher spatial resolution. As a result, detailed spatial information has become available. It has been found that spectral-spatial-based methods can provide good improvement in terms of classification accuracy (He *et al.* 2018). More and more spectral-spatial feature-based classification frameworks have been developed (Benediktsson *et al.* 2005; Camps-Valls *et al.* 2006), which incorporate the spatial contextual information into pixel-wise classifiers.

Recently, deep convolutional neural networks (DCNNs) have begun to dominate the classification of hyperspectral images, and manual

feature engineering has been replaced by automatic deep learning, such as with 3D-CNN (Y. Chen *et al.* 2016), CNN-PPF (W. Li *et al.* 2017), and DFFN (Song *et al.* 2018). Now, HSIC has entered a stage of 99% classification accuracy (Zhong *et al.* 2018; Paoletti *et al.* 2019). However, this high accuracy is achieved under the closed set assumption, in which the classes of all test samples are seen in training time. However, the closed set assumption is easily violated in HSIC, where collecting all possible classes for training is almost impossible. Due to budget limits, sample collection based on a field survey usually covers only a small portion of the study area, and only finite classes of interest are annotated (H. Chen *et al.* 2021). Classifiers with the closed set assumption are prone to errors with samples of unknown classes not of interest, and this limits their usability in HSIC. For example, if a closed set classifier is used to map certain crop types in a real HSI that contains other unknown land covers, it will inevitably overestimate crop area and therefore the total amount of food supplies.

In contrast, open set classification (OSC) assumes that for those test instances that do not belong to any known classes (seen by the classification model in training stage), the classifier must correctly identify them as an extra unknown class, as opposed to incorrectly classifying them as one of the known classes. Multi-class open set classification is challenging because it requires correct probability estimation of all known classes together with simultaneous precise refusal of unknown classes. To tackle this challenge, a number of approaches have been proposed for everyday images (Scheirer *et al.* 2013, 2014; Jain *et al.* 2014; Bendale and Boulton 2016; Ge *et al.* 2017; Yoshihashi *et al.* 2019). However, for HSI this research is just getting started. Only a few attempts have been made. Y. Liu *et al.* (2020) directly used OpenMax (Bendale and Boulton 2016) for open set HSIC. S. Liu *et al.* (2021) argued that the existing centroid-based method for everyday images was not suitable for few-shot HSIC, and proposed a multi-task deep-learning method based on the idea that the unknown should be poorly reconstructed using the classification feature.

In addition to few-shot mentioned by S. Liu *et al.* (2021), there are other notable differences between hyperspectral-image classification and everyday-image classification. First, the spatial resolution of hyperspectral images is much lower than that of everyday images, as hyperspectral images are remote sensing whereas everyday images are sensing at close range. For example, the India Pines data set, one of the most popular hyperspectral benchmarks, records 16 land cover classes in a region of 4350×4350 m² with a 30-m ground sampling distance. As a direct result of low spatial resolution, not all pixels in a hyperspectral image can be annotated with an explicit label. In this article, we borrow the term in the HSI unmixing task and divide the pixels of an HSI into two categories: pure and mixed; we deem only pure pixels suitable as examples for training a classification model. Second, there are more unlabeled than labeled pixels in the existing HSI data sets; for example, the Pavia University data set consists of 42 776 labeled pixels and 164 624 unlabeled pixels. These unlabeled pixels are ignored completely in existing HSIC work. Does that mean that unlabeled data are useless for classification tasks? Certainly not! In this article, we will use

Zhaolin Duan, Hao Chen, Xiaohua Li, and Jiliu Zhou are with the College of Computer Science, Sichuan University, Chengdu 610064, People's Republic of China (lxhw@scu.edu.cn).

Yuan Wang is with the Key Laboratory of Radiation Physics and Technology, Ministry of Education, Institute of Nuclear Science and Technology, Sichuan University, Chengdu 610064, People's Republic of China (wyuan@scu.edu.cn).

Contributed by Ruisheng Wang, September 10, 2021 (sent for review March 14, 2022; reviewed by Perpetual Akwensi, Bo Guo, Amr Abd-Elrahman).

Photogrammetric Engineering & Remote Sensing
Vol. 88, No. 10, October 2022, pp. 653–664.
0099-1112/22/653–664

© 2022 American Society for Photogrammetry
and Remote Sensing
doi: 10.14358/PERS.21-00067R3

**PEER-REVIEWED CONTENT
IS ONLY AVAILABLE TO
ASPRS MEMBERS AND SUBSCRIBERS**

**FOR MORE INFORMATION VISIT
[MY.ASPRS.ORG](https://my.asprs.org)**

**PEER-REVIEWED CONTENT
IS ONLY AVAILABLE TO
ASPRS MEMBERS AND SUBSCRIBERS**

**FOR MORE INFORMATION VISIT
MY.ASPRS.ORG**

**PEER-REVIEWED CONTENT
IS ONLY AVAILABLE TO
ASPRS MEMBERS AND SUBSCRIBERS**

**FOR MORE INFORMATION VISIT
[MY.ASPRS.ORG](https://my.asprs.org)**

**PEER-REVIEWED CONTENT
IS ONLY AVAILABLE TO
ASPRS MEMBERS AND SUBSCRIBERS**

**FOR MORE INFORMATION VISIT
MY.ASPRS.ORG**

**PEER-REVIEWED CONTENT
IS ONLY AVAILABLE TO
ASPRS MEMBERS AND SUBSCRIBERS**

**FOR MORE INFORMATION VISIT
[MY.ASPRS.ORG](https://my.asprs.org)**

**PEER-REVIEWED CONTENT
IS ONLY AVAILABLE TO
ASPRS MEMBERS AND SUBSCRIBERS**

**FOR MORE INFORMATION VISIT
MY.ASPRS.ORG**

**PEER-REVIEWED CONTENT
IS ONLY AVAILABLE TO
ASPRS MEMBERS AND SUBSCRIBERS**

**FOR MORE INFORMATION VISIT
[MY.ASPRS.ORG](https://my.asprs.org)**

**PEER-REVIEWED CONTENT
IS ONLY AVAILABLE TO
ASPRS MEMBERS AND SUBSCRIBERS**

**FOR MORE INFORMATION VISIT
MY.ASPRS.ORG**

**PEER-REVIEWED CONTENT
IS ONLY AVAILABLE TO
ASPRS MEMBERS AND SUBSCRIBERS**

**FOR MORE INFORMATION VISIT
[MY.ASPRS.ORG](https://my.asprs.org)**

**PEER-REVIEWED CONTENT
IS ONLY AVAILABLE TO
ASPRS MEMBERS AND SUBSCRIBERS**

**FOR MORE INFORMATION VISIT
MY.ASPRS.ORG**

**PEER-REVIEWED CONTENT
IS ONLY AVAILABLE TO
ASPRS MEMBERS AND SUBSCRIBERS**

**FOR MORE INFORMATION VISIT
[MY.ASPRS.ORG](https://my.asprs.org)**

The Fractional Vegetation Cover (FVC) and Associated Driving Factors of Modeling in Mining Areas

Jun Li, Tianyu Guo, Chengye Zhang, Fei Yang, and Xiao Sang

Abstract

To determine the fractional vegetation cover (FVC) and associated driving factors of modeling in mining areas, six types of data were used as driving factors and three methods—multi-linear regression (MLR), geographically weighted regression (GWR), and geographically weighted artificial neural network (GWANN)—were adopted in the modeling. The experiments, conducted in Shengli mining areas located in Xilinhote city, China, show that the MLR model without consideration of spatial heterogeneity and spatial non-stationarity performs the worst and that the GWR model presents obvious location differences, since it predefines a linear relationship which is unable to describe FVC for some locations. The GWANN model, improving on these defects, is the most suitable model for the FVC driving process in mining areas; it outperforms the other two models, with root-mean-square error (RMSE) and mean absolute percentage error (MAPE) reaching 0.16 and 0.20. It has improvements of approximately 24% in RMSE and 33% in MAPE compared to the MLR model, and those values grow to 59% and 71% when compared with the GWR model.

Introduction

Vegetation is the comprehensive result of the long-term interaction of hydrology, soil, landforms, climate variability, and human activities, and its composition, distribution, and development are closely related with multiple driving factors (Yang *et al.* 2011; Zhu *et al.* 2012; Y. Li *et al.* 2015). It plays a pivotal role in energy exchange processes, climate change, and hydrological and biogeochemical cycles on Earth's surface. Fractional vegetation cover (FVC) refers to the ratio of the vertical projection of vegetation (stems, branches, and leaves) in the statistical area of land surface (Purevdorj *et al.* 1998; Gitelson *et al.* 2002), which is a critical parameter measuring the vegetation coverage status and reflecting the degree of horizontal coverage of vegetation on land surface (Zhang *et al.* 2018). As quantitative information, FVC is not only used as a sensitive indicator to evaluate land degradation and desertification (C. Zhao *et al.* 2005) but also regarded as a controlling factor for universal soil loss equation, revised universal soil loss equation, and numerical climate and hydro-ecological models (Sellers *et al.* 1996; Qi *et al.* 2000; G. Wang *et al.* 2002; Wu *et al.* 2012).

With the continuous development of remote sensing technology, monitoring spatiotemporal and phenological variations of vegetation in a certain area, as well as estimating vegetation productivity based on remote sensing, has now become the main trend in the FVC research field (Okin *et al.* 2013; J. Li *et al.* 2019a; J. Li *et al.* 2020). Remote sensing has the advantages of wide coverage, high continuity, and comprehensiveness, which can provide measurement of FVC with a new direction (Xing *et al.* 2009; J. Peng *et al.* 2012; H. Liu *et al.*

2021). Among the remote sensing FVC estimation methods, the use of a vegetation index (VI)—which includes the enhanced vegetation index, the difference vegetation index, the ratio vegetation index, and the normalized difference vegetation index (NDVI)—is the most common method (Barati *et al.* 2011). Research has illustrated that the NDVI is very sensitive to the spatial distribution characteristics and growth state of vegetation (Tucker 1979); can to a great extent eliminate interference from topography, instruments, atmosphere, and so on; and has a significant linear correlation with FVC (Yuan *et al.* 2013; Zhang *et al.* 2018)—which all makes the NDVI currently the most widely used VI (Chen *et al.* 2014; Imukova *et al.* 2015). Specifically, the dimidiate pixel model based on the NDVI is a practical method to effectively estimate FVC, because of its simple calculations, easy interpretation, insensitivity to the effects of image radiometric correction, and independence from actual FVC data modeling (Mu *et al.* 2012; W. Peng *et al.* 2016; Z. Li *et al.* 2017).

In mining areas, the exploitation and use of mineral resources have changed the material cycle and energy flow of ecosystems, always resulting in serious vegetation degradation and environmental pollution (Fu *et al.* 2017). Therefore, there has been increasing attention given to environmental protection and ecological restoration in mining areas. Research has shown that study of the temporospatial characteristics and variations of vegetation coverage based on remote sensing technology is an effective way to reveal changes of the ecological environment in mining areas. Erener (2011) applied remote sensing-based vegetation cover monitoring to a case study of the Seyitömer Lignite Enterprise in Kütahya, Turkey, and successfully assessed the reclamation practices. G. Wang and Qiu (2018) extracted the FVC in the Huainan mining area from MODIS NDVI time-series products, analyzed the evolution of vegetation cover in the research area during the period of 2005–2014, and provided scientific references for the ecological restoration of the mining area. Fang *et al.* (2020) analyzed the spatiotemporal variation of vegetation coverage in a large-scale mining area in eastern Inner Mongolia, China, using the NDVI time series from 1982 to 2015, and explored the influencing factors before and after mining. J. Li *et al.* (2019b) unitized the long-term FVC based on NDVI data from 1985 to 2015 to evaluate the impact of coal mining and other human activities on land ecology at the Baorixile coal mining area in the heart of Hulunbeier in China.

The FVC in mining areas is affected by multiple driving factors, including topography, climate, and human activity. The influence of topography, especially altitude, can cause regional differences in the level of FVC as well as in its variation trend and fluctuation range (T. Zhao *et al.* 2019; H. Liu *et al.* 2021; Pang *et al.* 2021). Changes in temperature and precipitation directly affect vegetative photosynthesis, respiration, and soil organic carbon decomposition, among others, and then affect the growth distribution and evolution patterns of vegetation, which makes climate factors the dominant ones affecting FVC (J.

Jun Li, Tianyu Guo, Chengye Zhang, Fei Yang, and Xiao Sang are with the State Key Laboratory of Coal Resources and Safe Mining, China University of Mining and Technology-Beijing, Beijing, China; and the College of Geoscience and Surveying Engineering, China University of Mining and Technology-Beijing, Beijing, China (yangfei@cumtb.edu.cn).

Contributed by Ribana Roscher, September 22, 2021 (sent for review December 1, 2021; reviewed by Barry N. Haack, Yuki Hamada, Xiaofang Wei, Lukas Drees).

Photogrammetric Engineering & Remote Sensing
Vol. 88, No. 10, October 2022, pp. 665–671.
0099-1112/22/665-671

© 2022 American Society for Photogrammetry
and Remote Sensing
doi: 10.14358/PERS.21-00070R3

**PEER-REVIEWED CONTENT
IS ONLY AVAILABLE TO
ASPRS MEMBERS AND SUBSCRIBERS**

**FOR MORE INFORMATION VISIT
[MY.ASPRS.ORG](https://my.asprs.org)**

**PEER-REVIEWED CONTENT
IS ONLY AVAILABLE TO
ASPRS MEMBERS AND SUBSCRIBERS**

**FOR MORE INFORMATION VISIT
MY.ASPRS.ORG**

**PEER-REVIEWED CONTENT
IS ONLY AVAILABLE TO
ASPRS MEMBERS AND SUBSCRIBERS**

**FOR MORE INFORMATION VISIT
[MY.ASPRS.ORG](https://my.asprs.org)**

**PEER-REVIEWED CONTENT
IS ONLY AVAILABLE TO
ASPRS MEMBERS AND SUBSCRIBERS**

**FOR MORE INFORMATION VISIT
[MY.ASPRS.ORG](https://my.asprs.org)**

**PEER-REVIEWED CONTENT
IS ONLY AVAILABLE TO
ASPRS MEMBERS AND SUBSCRIBERS**

**FOR MORE INFORMATION VISIT
[MY.ASPRS.ORG](https://my.asprs.org)**

**PEER-REVIEWED CONTENT
IS ONLY AVAILABLE TO
ASPRS MEMBERS AND SUBSCRIBERS**

**FOR MORE INFORMATION VISIT
MY.ASPRS.ORG**

SUSTAINING MEMBERS

ACI USA Inc.

Weston, Florida
<https://acicorporation.com/>
 Member Since: 2/2018

Aerial Services, Inc.

Cedar Falls, Iowa
www.AerialServicesInc.com
 Member Since: 5/2001

Airworks Solutions Inc.

Boston, Massachusetts
 Member Since: 3/2022

Applanix

Richmond Hill, Ontario, Canada
<http://www.applanix.com>
 Member Since: 7/1997

Ayres Associates

Madison, Wisconsin
www.AyresAssociates.com
 Member Since: 1/1953

CT Consultants

Mentor, Ohio
 Member Since: 3/2022

Dewberry

Fairfax, Virginia
www.dewberry.com
 Member Since: 1/1985

Esri

Redlands, California
www.esri.com
 Member Since: 1/1987

GeoCue Group

Madison, Alabama
<http://www.geocue.com>
 Member Since: 10/2003

Geographic Imperatives LLC

Centennial, Colorado
 Member Since: 12/2020

GeoWing Mapping, Inc.

Richmond, California
www.geowingmapping.com
 Member Since: 12/2016

Half Associates, Inc.

Richardson, Texas
www.halff.com
 Member Since: 8/2021

Keystone Aerial Surveys, Inc.

Philadelphia, Pennsylvania
www.kasurveys.com
 Member Since: 1/1985

Kucera International

Willoughby, Ohio
www.kucerainternational.com
 Member Since: 1/1992

L3Harris Technologies

Broomfield, Colorado
www.l3harris.com
 Member Since: 6/2008

Merrick & Company

Greenwood Village, Colorado
www.merrick.com/gis
 Member Since: 4/1995

Nearmap

South Jordan, Utah
www.nearmap.com
 Member Since: 6/2023

NV5 Geospatial

Sheboygan Falls, Wisconsin
www.quantumspatial.com
 Member Since: 1/1974

Pickett and Associates, Inc.

Bartow, Florida
www.pickettusa.com
 Member Since: 4/2007

Riegl USA, Inc.

Orlando, Florida
www.rieglusa.com
 Member Since: 11/2004

Robinson Aerial Surveys, Inc.(RAS)

Hackettstown, New Jersey
www.robinsonaerial.com
 Member Since: 1/1954

Sanborn Map Company

Colorado Springs, Colorado
www.sanborn.com
 Member Since: 10/1984

Surdex Corporation

Chesterfield, Missouri
www.surdex.com
 Member Since: 12/2011

Surveying And Mapping, LLC (SAM)

Austin, Texas
www.sam.biz
 Member Since: 12/2005

T3 Global Strategies, Inc.

Bridgeville, Pennsylvania
<https://t3gs.com/>
 Member Since: 6/2020

Terra Remote Sensing (USA) Inc.

Bellevue, Washington
www.terraremote.com
 Member Since: 11/2016

Towill, Inc.

San Francisco, California
www.towill.com
 Member Since: 1/1952

Woolpert LLP

Dayton, Ohio
www.woolpert.com
 Member Since: 1/1985

SUSTAINING MEMBER BENEFITS

Membership

- ✓ Provides a means for dissemination of new information
- ✓ Encourages an exchange of ideas and communication
- ✓ Offers prime exposure for companies

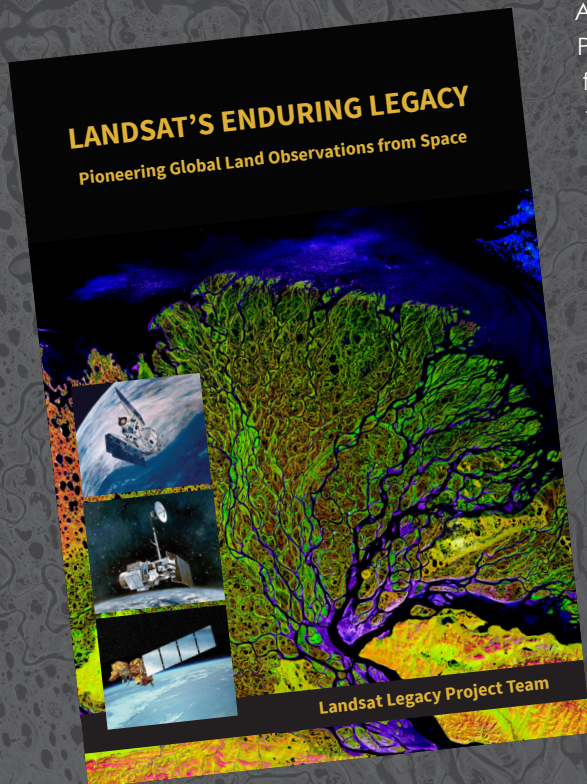
Benefits of an ASPRS Membership

- Complimentary and discounted Employee Membership*
- E-mail blast to full ASPRS membership*
- Professional Certification Application fee discount for any employee
- Member price for ASPRS publications
- Discount on group registration to ASPRS virtual conferences
- Sustaining Member company listing in ASPRS directory/website
- Hot link to company website from Sustaining Member company listing page on ASPRS website
- Press Release Priority Listing in PE&RS Industry News
- Priority publishing of Highlight Articles in PE&RS plus, 20% discount off cover fee
- Discount on PE&RS advertising
- Exhibit discounts at ASPRS sponsored conferences (exception ASPRS/ILMF)
- Free training webinar registrations per year*
- Discount on additional training webinar registrations for employees
- Discount for each new SMC member brought on board (Discount for first year only)

*quantity depends on membership level

LANDSAT'S ENDURING LEGACY

PIONEERING GLOBAL LAND OBSERVATIONS FROM SPACE



After more than 15 years of research and writing, the Landsat Legacy Project Team published, in collaboration with the American Society for Photogrammetry and Remote Sensing (ASPRS), a seminal work on the nearly half-century of monitoring the Earth's lands with Landsat. Born of technologies that evolved from the Second World War, Landsat not only pioneered global land monitoring but in the process drove innovation in digital imaging technologies and encouraged development of global imagery archives. Access to this imagery led to early breakthroughs in natural resources assessments, particularly for agriculture, forestry, and geology. The technical Landsat remote sensing revolution was not simple or straightforward. Early conflicts between civilian and defense satellite remote sensing users gave way to disagreements over whether the Landsat system should be a public service or a private enterprise. The failed attempts to privatize Landsat nearly led to its demise. Only the combined engagement of civilian and defense organizations ultimately saved this pioneer satellite land monitoring program. With the emergence of 21st century Earth system science research, the full value of the Landsat concept and its continuous 45-year global archive has been recognized and embraced. Discussion of Landsat's future continues but its heritage will not be forgotten.

The pioneering satellite system's vital history is captured in this notable volume on Landsat's Enduring Legacy.

Landsat Legacy Project Team

Samuel N. Goward
Darrel L. Williams
Terry Arvidson
Laura E. P. Rocchio
James R. Irons
Carol A. Russell
Shaida S. Johnston

Landsat's Enduring Legacy

Hardback, 2017, ISBN 1-57083-101-7

Member/Non-member \$48*

Student Member \$36*

* Plus shipping

Order online at
www.asprs.org/landsat



asprs THE IMAGING & GEOSPATIAL
INFORMATION SOCIETY

LEARN
DO
GIVE
BELONG

ASPRS Offers

- » Cutting-edge conference programs
- » Professional development workshops
- » Accredited professional certifications
- » Scholarships and awards
- » Career advancing mentoring programs
- » *PE&RS*, the scientific journal of ASPRS

asprs.org

ASPRS